UC San Diego
UC San Diego Electronic Theses and Dissertations

Title

Experimental Studies of Multi-Species Pure Ion Plasmas: Cyclotron Modes, Long-Range Collisional Drag, and Non-Linear Langmuir Waves

Permalink

https://escholarship.org/uc/item/2458h91n

Author

Affolter, Matthew

Publication Date

2016

Peer reviewed|Thesis/dissertation

eScholarship.org Powered by the California Digital Library
University of California

UNIVERSITY OF CALIFORNIA, SAN DIEGO

Experimental Studies of Multi-Species Pure Ion Plasmas: Cyclotron Modes, Long-Range Collisional Drag, and Non-Linear Langmuir Waves

A dissertation submitted in partial satisfaction of the
requirements for the degree
Doctor of Philosophy

in

Physics

by

Matthew Affolter

Committee in charge:

Professor C. Fred Driscoll, Chair
Professor Robert E. Continetti
Professor Daniel H. E. Dubin
Professor Clifford M. Surko
Professor George R. Tynan

2016

Copyright
Matthew Affolter, 2016
All rights reserved.

The dissertation of Matthew Affolter is approved, and it is acceptable in quality and form for publication on microfilm and electronically:

Chair

University of California, San Diego

2016

DEDICATION

To my parents, Bob and Mandy, and my grandfather, Frank Wilson,
for the many years of support and encouragement.

EPIGRAPH

The desire for knowledge shapes a man.

—Patrick Rothfuss, *The Wise Man's Fear*

TABLE OF CONTENTS

LIST OF FIGURES

LIST OF TABLES

ACKNOWLEDGEMENTS

First and foremost, I would like to thank Dr. Fred Driscoll and Dr. Francois Anderegg. I started graduate school with very little experimental expertise, and it was only through their guidance that I became the experimentalist I am today. Dr. Driscoll, my advisor, constantly challenged me to focus on the fundamentals of the problem. He taught me the type of critical thinking that is required to be a good experimentalist. The sum of my knowledge of optics, vacuum technology, and electronic repair I owe to the patient and lucid explanations of Dr. Anderegg. He was always willing to explain the basics, and taught me good experimental practices.

I also owe a debt of gratitude to the group theorists Dr. Tom O'Neil and Dr. Dan Dubin. My decision to studying plasma physics was heavily influenced by my first year electrodynamics course taught by Dr. O'Neil, and I am grateful that I made that decision. Most of the theory in this dissertation comes from Dr. Dubin. He was always available to answer questions, and help interpret the experimental results.

Lastly, I would like to thank my family and friends. My parents who have always been supportive of my endeavors. I would not have made it this far without your encouragement. My brother Ben for getting me to take time off to hangout; it is always fun to beat you at fishing. And Cody Chapman, my roommate and fellow graduate student, for taking my mind off work with ridiculous TV and hours of playing Skyrim ("what a waste").

This research was supported financially by the National Science Foundation Grant PHY-1414570, and the Department of Energy Grants DE-SC0002451 and DE-SC0008693.

Chapters 2 and 3, in part, are a reprint of the material as it appears in three journal articles: M. Affolter, F. Anderegg, D. H. E. Dubin, and C. F. Driscoll, *Physics Letters A*, **378**, 2406 (2014); M. Affolter, F. Anderegg, D.H.E. Dubin and C.F. Driscoll, *Physics of Plasmas*, **22**, 055701 (2015); and M. Affolter, F. Anderegg, C.F. Driscoll, *Journal of the American Society for Mass Spectrometry*, **26**, 330 (2015). The dissertation author was the primary investigator and author of these papers.

Chapter 4, in part, is currently being prepared for submission for publication. M. Affolter, F. Anderegg, D.H.E. Dubin and C.F. Driscoll. The dissertation author was the primary investigator and author of this material.

Chapter 5, in part, is currently being prepared for submission for publication. M. Affolter, F. Anderegg, D.H.E. Dubin, F. Valentini and C.F. Driscoll. The dissertation author was the primary investigator and author of this material.

VITA

2008	B. S. in Physics, Western Washington University
2009	M. S. in Physics, University of California, San Diego
2008-2009	Teaching Assistant, Department of Physics, University of California, San Diego
2009-2016	Research Assistant, Department of Physics, University of California, San Diego
2016	Ph. D. in Physics, University of California, San Diego

PUBLICATIONS

M. Affolter, F. Anderegg, D.H.E. Dubin, and C.F. Driscoll, "Cyclotron Mode Frequencies and Resonant Absorption in Multi-species Ion Plasmas", *Physics of Plasmas*, **22**, 055701 (2015)

M. Affolter, F. Anderegg, and C.F. Driscoll, "Space Charge Frequency Shifts of the Cyclotron Modes in Multi-Species Ion Plasmas", *J. Am. Soc. Mass Spectrom.*, **26**, 330 (2015)

F. Anderegg, M. Affolter, A. Ashourvan, D.H.E. Dubin, F. Valentini, and C.F. Driscoll, "Non-Linear Plasma Wave Decay to Longer Wavelength", *Non-Neutral Plasma Physics IX*, AIP Conf. Proc., **1668**, 020001 (2015)

M. Affolter, F. Anderegg, D.H.E. Dubin, and C.F. Driscoll, "Cyclotron Mode Frequency Shifts in Multi-species Ion Plasmas", *Physics Letters A*, **378**, 2406 (2014)

M. Affolter, F. Anderegg, C.F. Driscoll, and D.H.E. Dubin, "Cyclotron Resonances in a Non-Neutral Multispecies Ion Plasma", *Non-Neutral Plasma Physics VIII*, AIP Conf. Proc., **1521**, 175-183 (2013)

ABSTRACT OF THE DISSERTATION

Experimental Studies of Multi-Species Pure Ion Plasmas: Cyclotron Modes, Long-Range Collisional Drag, and Non-Linear Langmuir Waves

by

Matthew Affolter

Doctor of Philosophy in Physics

University of California, San Diego, 2016

Professor C. Fred Driscoll, Chair

Cyclotron modes are studied on rigid rotor, multi-species ion plasmas confined in a Penning-Malmberg trap. Collective effects and radial electric fields shift the cyclotron mode frequencies away from the "bare" cyclotron frequencies $2\pi F_c^{(s)} \equiv (q_s B/M_s c)$ for each species s. These frequency shifts are measured on the distinct cyclotron modes ($m_\theta = 0, 1,$ and 2) with $\cos(m_\theta \theta)$ azimuthal dependence. We find that the frequency shifts corroborate a simple theory expression in which collective effects enter only through the $E \times B$ rotation frequency f_E and the species fraction δ_s, when the plasma is radially uniform. At ultra-low temperatures, these plasmas exhibit centrifugal separation by mass, and additional frequency shifts are observed in agreement with a more general theory. Additionally, quantitative measurements of the plasma heating from short resonant cyclotron bursts are found to be proportional to the species fraction.

These cyclotron modes are used as a diagnostic tool to estimate the plasma composition, in order to investigate the damping of Langmuir waves due to inter-species collisions. Experiments and theory of this collisional inter-species drag damping are presented. This also provides the first experimental confirmation of recent theory predicting enhanced collisional slowing due to long-range collisions. Drag damping theory, proportional to the collisional slowing rate, is in quantitative agreement with the experimental results only when these long-range collisions are included, exceeding classical collision calculations by as much as an order of magnitude.

At large wave amplitudes, Langmuir waves exhibit harmonic generation, nonlinear frequency shifts, and a parametric decay instability, which are experimentally investigated. The parametric wave-wave coupling rates are in agreement with three-wave instability theory in the dispersion dominated oscillatory coupling regime, and in the phase-locked exponential decay regime. However, significant variations are observed near the decay threshold, including slow, oscillatory growth of the daughter wave amplitude. These experimental results have motivated wide-ranging theory and simulations, which provide both insights and puzzles.

Chapter 1

Introduction and Overview

Plasmas consisting of a single sign of charge, commonly referred to as non-neutral plasmas, possess the important property that they can be confined in a state of global thermal equilibrium by a combination of static electric and magnetic fields, called a Penning-Malmberg trap [1]. The thermal equilibrium state is characterized by the plasma temperature T, density n_0, and radius R_p. These plasmas are well controlled and diagnosed, enabling precise measurements of many physical processes over a wide range of densities and temperatures.

Non-neutral ion plasmas are used to study a broad range of physics including quantum simulations [2], spectroscopy [3], and basic plasma physics [4]. Rarely do these pure ion plasmas consist of a single-species. Plasma sources routinely contain multiple species and isotopes [5, 6], and unwanted impurity ions often arise from ionization and chemical reactions with the neutral background gas [7, 8, 9]. These impurities are difficult to diagnose, and they introduce complex multi-species plasma phenomena. The majority of this dissertation is concerned with methods of diagnosing these impurities, and on the multi-species effects they introduce.

Chapter 2 presents the details of the IV apparatus [5] on which these experiments are conducted. This is a laser-diagnosed Penning-Malmberg trap with a Magnesium plasma source. A brief overview of the trap geometry and "rotating-wall" technique will be discussed, along with details of the laser diagnostics and cooling of these ion plasmas.

Methods of diagnosing the species fractions through cyclotron modes are presented in Chapter 3. We will describe a new laser-thermal cyclotron spectroscopy technique, which detects mode resonances at very low amplitudes. This technique enables detailed observations of surface cyclotron modes with $m_\theta = 0$, 1, and 2. For each species s, we observe cyclotron mode frequency shifts that depend on the plasma density through the rotation frequency, and on the charge concentration of species s, in close agreement with recent theory. This includes the novel $m_\theta = 0$, radial "breathing" mode, which generates no external electric field except at the plasma ends. These cyclotron frequency shifts can be used to determine the plasma rotation frequency and the species charge concentrations, in close agreement with our laser diagnostics. These new results give a physical basis for the "space charge" and "amplitude" calibration equations of cyclotron mass spectroscopy [10], widely used in molecular chemistry and biology.

In Chapter 4, damping measurements of small amplitude Langmuir waves are presented, spanning a range of four decades in temperature. These Langmuir waves are θ-symmetric, standing plasma oscillations discretized by the axial wavenumber $k_z = m_z\pi/L_p$. At high temperatures ($T \sim 0.5$ eV), these axial plasma waves are Landau damped [11], but this prototypical Landau damping becomes exponentially weak for $T \lesssim 0.2$ eV. However, we believe that Landau damping is extended to a lower temperature regime ($0.02 \lesssim T \lesssim 0.2$ eV) through the same Landau interaction acting on "bounce-harmonics" of the wave, caused by finite-length effects. The primary interest of this chapter will be on the low temperature regime ($T \lesssim 10^{-2}$ eV) where the damping scales roughly as $T^{-3/2}$ and is dependent on the plasma composition, suggesting inter-species drag as the damping mechanism.

This inter-species drag damping provides a test of recent collision theory [12], which predicts that the parallel slowing rate of these magnetized plasmas is enhanced through long-range collisions. Drag damping theory, proportional to the parallel slowing rate, is presented. We find that this drag damping theory is in quantitative agreement with the experimental results only when long-range collisions are included, exceeding classical collision calculations by as much as an order of magnitude.

The non-linear effects of frequency shifts, harmonic content, and instability of large amplitude Langmuir waves are presented in Chapter 5. We characterize non-linear frequency shifts and Fourier harmonic content versus amplitude, both of which are increased when the wave dispersion is made more nearly acoustic. Non-linear coupling rates are measured between large amplitude $m_z = 2$ waves and small amplitude $m_z = 1$ waves, which have a small frequency detuning $\Delta\omega \equiv 2\omega_1 - \omega_2$. At small excitation amplitudes, this detuning causes the $m_z = 1$ mode amplitude to "bounce" at rate $\omega_B \approx \Delta\omega$, with amplitude excursions $A_1 \propto \delta n_2/n_0$ in quantitative agreement with cold fluid theory [13] and Vlasov simulations. At larger excitation amplitudes, where the non-linear coupling rate exceeds the detuning, phase-locked exponential growth of the $m_z = 1$ mode is observed, consistent with the three-wave instability theory [13]. Significant variations are observed experimentally near the decay threshold, including an average growth of the daughter wave amplitude before the phase-locked regime. A recent cold fluid analysis [14] that considers frequency harmonics of these large amplitude waves give stunningly divergent instability predictions that depend sensitively on the dispersion-moderated harmonic content.

Chapter 2

Experimental Apparatus

2.1 IV Apparatus

These experiments are conducted on pure ion plasmas confined in a Penning-Malmberg trap, as shown in Fig. 2.1. A Magnesium vacuum electrode arc [15] creates a neutralized plasma, and the free electrons stream out through the +180 V end confinement potentials, leaving $N_{tot} \sim 2 \times 10^8$ ions in a cylindrical column with a length $L_p \sim 10$ cm. Radial confinement is provided by the axial magnetic field $B = 2.965 \pm 0.002$ Tesla $(-\hat{z})$. The ions are predominately Mg^+ in three isotopic states, with natural abundances 79% $^{24}\mathrm{Mg}^+$, 10% $^{25}\mathrm{Mg}^+$, and 11% $^{26}\mathrm{Mg}^+$. Other impurity ions, mostly of $\mathrm{H_3O}^+$, arise from chemical reactions with the background gas. By changing the background gas pressure over the range $10^{-10} \leq P \leq 10^{-8}$ Torr, the impurity ion fraction is varied from $5 - 30\%$.

A "rotating wall" (RW) technique [16] utilizes azimuthally rotating wall voltages to maintain the plasma in a near rigid-rotor equilibrium state for days. By altering the frequency of this RW, the plasma can be arranged to a desired density n_0, rotation

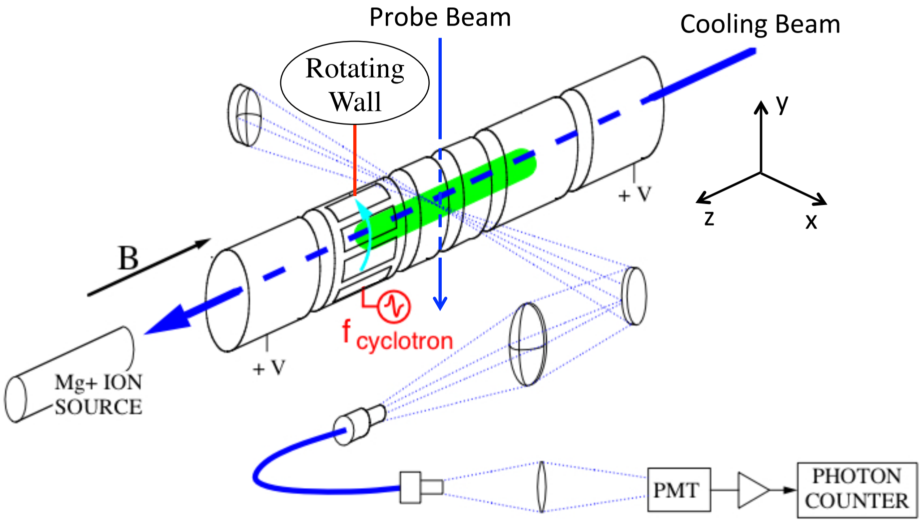

Figure 2.1: Schematic diagram of the IV apparatus. A cylindrical Penning-Malmberg trap with "rotating wall" and laser diagnostics.

frequency $f_E \equiv \mathrm{v}_\theta / r$, and radius R_p. The ion densities range over $n_0 = (0.9 \rightarrow 6.4) \times 10^7 \text{ cm}^{-3}$, with rotation rates $f_E = (4 \rightarrow 31)$ kHz, and inversely varying radii $R_p = (6 \rightarrow 3)$ mm. The plasma length L_p and wall radius $R_w = 2.86$ cm remain fixed.

2.2 Laser Diagnostics

Detailed measurements of these Mg^+ plasmas are obtained from laser induced fluorescence techniques [5]. Figure 2.2 diagrams the Mg^+ atomic energy levels, and the two cyclic transitions that are in the near UV ($\lambda \sim 280$ nm). In these experiments, we use the $3\mathrm{S}_{1/2}, \mathrm{m}_j = -1/2 \rightarrow 3\mathrm{P}_{3/2}, \mathrm{m}_j = -3/2$ transition (blue dashed arrow) at a frequency $f_0 \sim 1.1 \times 10^{15}$ Hz for laser diagnostics. A tunable, CW dye laser is frequency-doubled to create a UV probe beam, which can be sent through the plasma either perpendicular or parallel to the magnetic field. The frequency f_L of this probe beam is scanned over the Doppler-broadened atomic transition of each Mg^+ isotope. The excited ion state decays immediately and the resulting fluorescence photons are

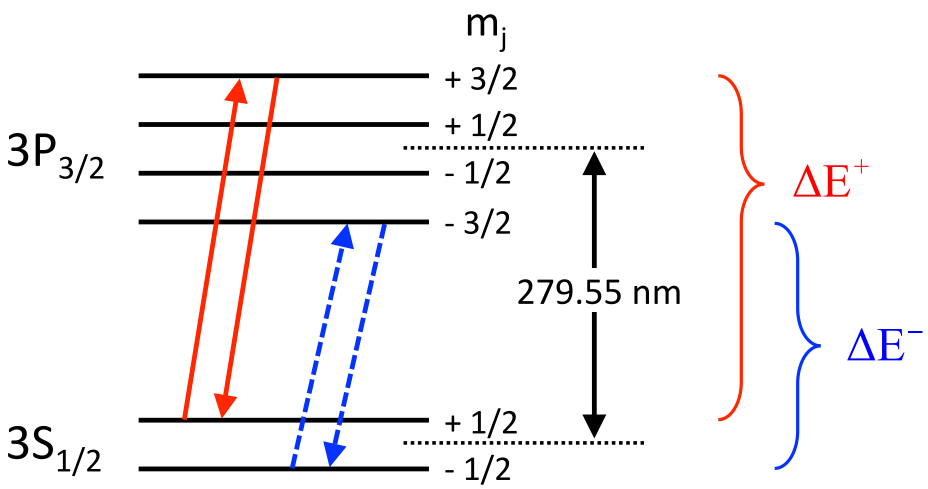

Figure 2.2: Energy level diagram of a Mg$^+$ ion. The Zeeman effect splits the 3S$_{1/2}$ and 3P$_{3/2}$ levels (dotted) into magnetic field dependent energy states. The arrows illustrate the cyclic transitions used for laser diagnostics and cooling (blue dashed), and for magnetic field calibration (red/blue).

counted using a photomultiplier tube. From this detected photon count rate, we construct the Mg$^+$ velocity distribution.

Figure 2.3 shows raw data and 3-isotope Voigt fits to the typical Mg$^+$ distributions resulting from a perpendicular probe laser scan at three radial ($\hat{x}$) locations in the plasma. For $r > 0$, the velocity distributions are positively and negatively detuned from the $\mathrm{v}_\theta = 0$ resonance due to a Doppler shift from the plasma rotation, either away from or towards the probe laser beam in the $(-\hat{y})$ direction. This detuning is a direct measurement of the $E \times B$ rotation profile $\mathrm{v}_\theta(r)$. Radial profiles of the plasma temperature $T(r)$ and Mg$^+$ density $n_{\mathrm{Mg}}(r)$ can also be obtained by fitting the velocity distribution at each radial location with Voigt distributions for each Mg$^+$ isotope.

Shown in Fig. 2.4 are the measured density and rotation profiles (symbols) at three different rotation rates. These profiles are a convolution of the true “top-hat” plasma profile with the finite size (Δx half-width $\sigma_L \sim 0.39$ mm) probe laser beam. We obtain the true plasma radius R_p and rotation frequency f_E by fitting to a convolved

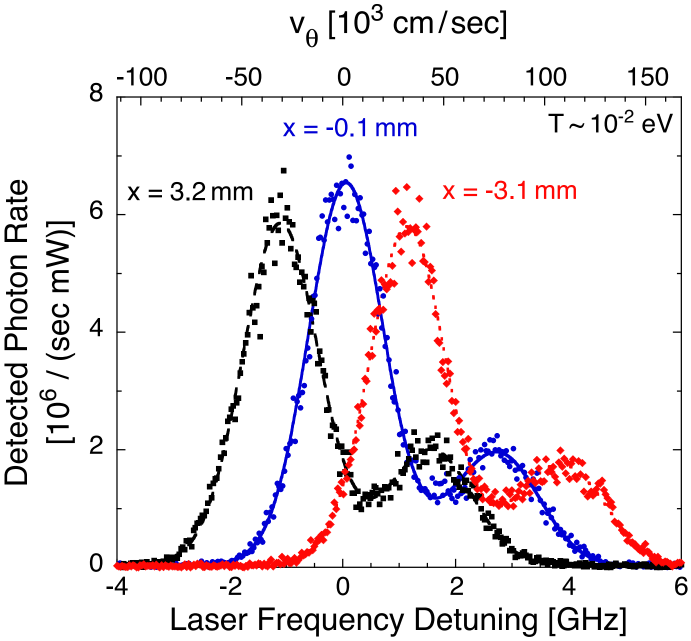

Figure 2.3: Data and fits of the LIF measured Mg^+ velocity distributions at three radial locations $r \equiv |x|$ in the plasma. At each location, the larger peak is the distribution of $^{24}\mathrm{Mg}^+$, and the smaller hump is the combined distributions of $^{25}\mathrm{Mg}^+$ and $^{26}\mathrm{Mg}^+$.

"top-hat" model with constant $n(r) = n_{\mathrm{Mg}}$ and $\mathrm{v}_\theta(r) = 2\pi r f_E$ for $r \leq R_p$, giving the dashed curves in Fig. 2.4. The solid lines in Fig. 2.4 are the resulting true "top-hat" Mg^+ density and rigid-rotor rotation profiles of the plasma. This rigid-rotor rotation frequency f_E is a direct measurement of the total electric field strength from ion space charge and trap potentials.

2.3 RZ Poisson-Boltzmann Solver

A RZ Poisson-Boltzmann solver extends these measured radial cross-sections to determine the plasma length. This solver iterates the RZ density $n(r, z)$ to establish

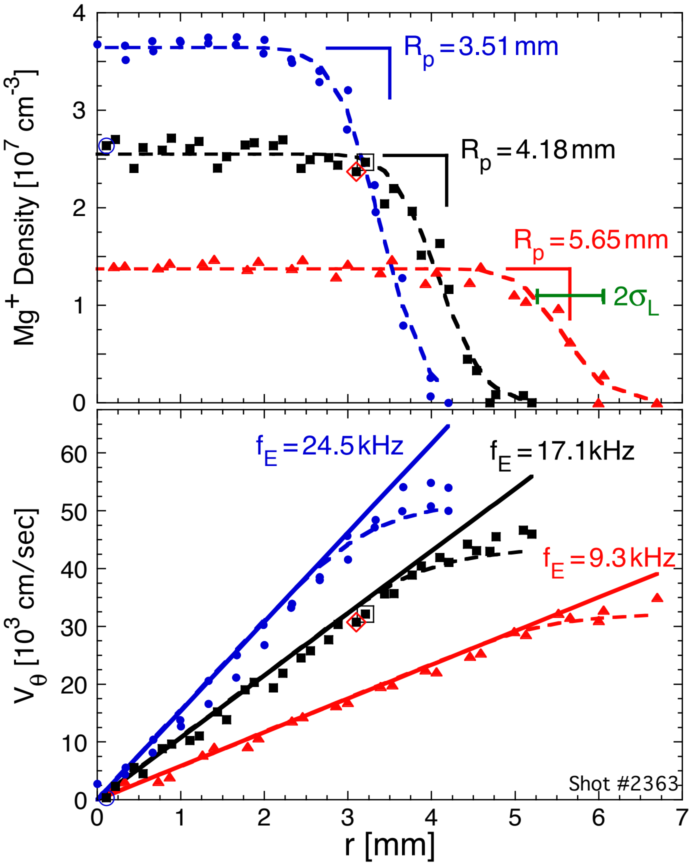

Figure 2.4: Radial profiles of Mg^+ density (Top) and rotation velocities (Bottom) at three different rotation rates for a $T \sim 10^{-2}$ eV plasma. Symbols are laser-width-averaged data, and dashed curves are fits to the "top-hat" rigid-rotor model (solid lines). The three circled/boxed data points correspond to the LIF signals of Fig. 2.3.

a self-consistent solution of Poisson's equation,

$$\nabla^2\phi(r,z) = -4\pi q n(r,z), \tag{2.1}$$

given the boundary conditions of the confining potentials. The boundary conditions at $r = R_w$ match the experimental setup. The z-boundary condition is taken to be $\partial\phi/\partial z = 0$ at $z = \pm z_E$, where z_E is well beyond the plasma end.

Local thermal equilibrium along the magnetic field (i.e. along $\hat{z}$) is assumed, so that the density

$$n(r,z) = S(r)\exp[-q\phi(r,z)/T(r)]. \tag{2.2}$$

Here $T(r)$ is directly measured, and $S(r)$ is constrained by the measured radial density profile $n(r,z_L) = n_0(r)$, where $z_L = L_p/2$ is the axial position of the probe laser beam.

Equation 2.1 is solved numerically on a 512 × 1024 grid using an iterative calculation. Initially, the plasma is assumed to be a rod of charge $n(r, 0 \leq z \leq L_{conf}) = n_0(r)$ extending the length of the confining volume L_{conf}. This initial guess is used with the boundary conditions to determine $\phi(r,z)$, which is then used to determine a new guess of $n(r,z)$. A fraction of this new $n(r,z)$ solution is added to the old solution while maintaining the constraint that $n(r,z_L) = n_0(r)$. This process is repeated until the maximum density change is less than 0.01%. The resulting solutions are cylindrical plasmas of about 10 cm in length with rounded ends.

2.4 Laser Cooling

A benefit of using Mg^+ ions is that the plasma temperature can be controlled through laser cooling on a cyclic transition (blue dashed arrow of Fig. 2.2) with the rest-frame resonance ω_0. An ion moving with velocity v is then resonant at a laser frequency $\omega(\vec{v}) = \omega_0 + \vec{k} \cdot \vec{v}$, where $\vec{k} = \omega_0/c$ is the laser wavenumber. By tuning the axial cooling laser ($\pm\hat{z}$) to a frequency slightly below ω_0, ions moving with a specific velocity v_c towards the laser will be resonantly excited, and receive a momentum "kick" decreasing the ion velocity. These excited ions will then remit a photon in a random direction. On average, this absorbtion/emission cycle results in a reduction in the ions velocity, and thus cooling of the plasma along the parallel ($\hat{z}$) degree of freedom. Perp-to-parallel collisions at a rate $\nu_{\perp\parallel}$ then cool the perpendicular degree of freedom.

In these experiments, the plasma temperature is controlled over the range ($10^{-5} \to 1$) eV through laser cooling of the $^{24}\mathrm{Mg}^+$ ions. This corresponds to a several decade change in the perp-to-parallel collisionality $\nu_{\perp\parallel} = (10^4 \to 1)\ s^{-1}$, and in the Debye length $\lambda_D = (0.005 \to 1.7)$ mm. The radial distribution of ion species is also temperature dependent through the effect of centrifugal mass separation [17, 18, 19, 20]. For plasmas at $T \gtrsim 10^{-2}$ eV, the ions species are uniformly mixed. In contrast, at $T < 10^{-3}$ eV, the species begin to centrifugally separate by mass, with near-complete separation at $T < 10^{-4}$ eV. This is discussed in Section 3.6.

2.5 Magnetic Field Calibration

Chapter 3 of this dissertation deals with cyclotron mode frequency shifts on the order of a percent of the "bare" cyclotron frequency. To understand these frequency shifts, we calibrated the magnetic field strength in the confinement volume by measuring the Zeeman splitting of the Mg^+ atomic levels. As shown in Fig. 2.2, the atomic energy levels are split, and this spacing is dependent on the magnetic field strength. The energy (or frequency) difference between the two cyclic transition, illustrated by the arrows in Fig. 2.2, is

$$\Delta E_Z \equiv \Delta E^+ - \Delta E^- = h\Delta f_Z = 28.0136\, h\, B\, [\text{GHz/Tesla}]. \tag{2.3}$$

A 120 GHz scan in the UV covering these two cyclic transitions finds $\Delta f_Z = 83.06 \pm 0.06$ GHz, corresponding to a magnetic field strength of $B = 2.965 \pm 0.002$ Tesla. This 10^{-3} accuracy is maintained for all experiments.

2.6 Acknowledgements

This chapter, in part, is a reprint of the material as it appears in three journal articles: M. Affolter, F. Anderegg, D. H. E. Dubin, and C. F. Driscoll, *Physics Letters A*, **378**, 2406 (2014); M. Affolter, F. Anderegg, D.H.E. Dubin and C.F. Driscoll, *Physics of Plasmas*, **22**, 055701 (2015); and M. Affolter, F. Anderegg, C.F. Driscoll, *Journal of the American Society for Mass Spectrometry*, **26**, 330 (2015). The dissertation author was the primary investigator and author of these papers.

Chapter 3

Cyclotron Mode Frequencies and Resonant Absorption

3.1 Introduction

Plasmas exhibit a variety of cyclotron modes, which are used in a broad range of devices to manipulate and diagnose charged particles. In fusion devices, cyclotron modes are used for plasma heating [21, 22, 23], and the intensity of the plasma cyclotron emission provides a diagnostic of the plasma temperature [24, 25]. Cyclotron modes in ion clouds are widely used in molecular chemistry and biology to precisely measure ion mass. In these plasmas, with a single sign of charge [26, 27, 28], collective effects and electric fields shift the cyclotron mode frequencies away from the "bare" cyclotron frequencies $2\pi F_c^{(s)} \equiv (q_s B/M_s c)$ for each species s. Mass spectroscopy devices typically attempt to mitigate these effects with the use of calibration equations, but these equation commonly neglect collective effects [29] or conflate them with amplitude effects [27].

Here we quantify the shifts of cyclotron mode frequencies for several cyclotron modes varying as $\cos(m_\theta \theta - 2\pi f_{m_\theta}^{(s)} t)$. The $m_\theta = 1$ mode represents an orbit of the center-of-mass, and is the most commonly utilized mode. We also quantify the plasma heating from resonant wave absorption of the $m_\theta = 1$ mode. These measurements are conducted on well-controlled, laser-diagnosed, multi-species ion plasmas, with near uniform charge density n_0 characterized by the near-uniform $E \times B$ rotation frequency $f_E \equiv cen_0/B$. On these radially uniform plasmas, the cyclotron mode frequency shifts are proportional to f_E, with a constant of proportionality dependent on the species fraction $\delta_s \equiv n_s/n_0$, as predicted by the simple theory expression [7, 30, 31] of Eq. 3.4. The plasma heating from resonant wave absorption is analyzed quantitatively using a center-of-mass model. We find that the plasma heating and cyclotron mode frequency shifts can be used as diagnostic tools to measure the species fractions δ_s.

The cyclotron mode frequencies are also investigated on plasmas with non-uniform species distributions $n_s(r)$. The radial distribution of species is controlled through the effects of centrifugal mass separation [17, 18, 19, 20]. When the species are well separated radially, each cyclotron mode frequency depends on the "local" concentration of that species. These measurements are in agreement with a more general theory [30, 31] involving a radial integral over $n_s(r)$, with a simple asymptote for complete separation into distinct annuli.

3.2 Thermal Cyclotron Spectroscopy

Thermal Cyclotron Spectroscopy (TCS) is used to detect the cyclotron resonances. A cartoon of this process is shown in the inset of Fig. 3.1. A series of RF bursts, scanned over frequency, are applied to an azimuthally sectored confinement ring.

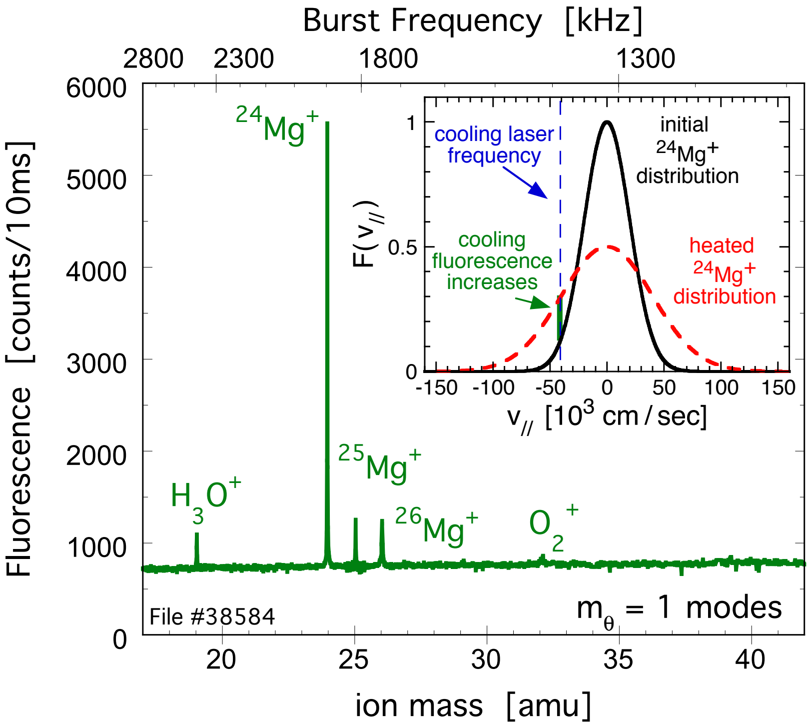

Figure 3.1: Broad TCS scan of a typical plasma containing $^{24}\mathrm{Mg}^+$, $^{25}\mathrm{Mg}^+$, and $^{26}\mathrm{Mg}^+$; with $\mathrm{H_3O}^+$ and O_2^+ impurity ions. This mass spectra is obtained by monitoring the plasma heating from resonant wave absorption through the cooling laser fluorescence, as depicted in the inset cartoon.

Resonant wave absorption heats the plasma, changing the $^{24}\mathrm{Mg}^+$ velocity distribution, which is detected through LIF diagnostics.

Figure 3.1 shows a broad TCS scan used to identify the composition of a “dirty” plasma. Here the plasma heating is detected as an increase in the cooling fluorescence, and we use a long RF burst of 10^4 cycles to obtain a narrow frequency resolution. As expected, the plasma consist of $^{24}\mathrm{Mg}^+$, and the Magnesium isotopes $^{25}\mathrm{Mg}^+$ and $^{26}\mathrm{Mg}^+$. Ions of mass 19 amu and 32 amu are also typically observed, which we believe to be $\mathrm{H_3O}^+$ and O_2^+, resulting from ionization and chemical reactions with the background gas at a pressure of $P \sim 10^{-9}$ Torr. Typical “dirty” plasma isotopic charge fractions are $\delta_{24} = 0.54$, $\delta_{25} = 0.09$, $\delta_{26} = 0.10$, with the remaining 27% a mixture of $\mathrm{H_3O}^+$ and

O_2^+.

3.3 Resonant Heating

To quantify the resultant heating from resonant wave absorption, we measure the time evolution of the parallel velocity distribution $F(\mathrm{v}_\parallel, t)$ concurrent with a resonant RF burst. This entails detuning the probe laser frequency to a $\mathrm{v}_\parallel$ in the Mg^+ distribution. The cooling beam is then blocked, a cyclotron mode is excited, and the arrival time of each detected photon is recorded. By repeating this process for 100 different probe detuning frequencies (i.e. parallel velocities), $F(\mathrm{v}_\parallel, t)$ is measured for specified time bins. These distributions are fit by Maxwellian distributions to construct the time evolution of the plasma temperature.

Figure 3.2 shows the resulting temperature evolution for the excitation of the center-of-mass mode of $^{24}\mathrm{Mg}^+$ at three different burst amplitudes A_B. In this case, the plasma is initially cooled to $T \sim 10^{-3}$ eV, and the heating due to collisions with the room temperature background gas is negligible, at about 1.7×10^{-6} eV/ms. At 20 ms, the cyclotron mode is excited using a 200 cycle burst at $f_1^{(24)} = 1894.6$ kHz, corresponding to a burst period $\tau_B = 0.1$ ms. The plasma temperature increases by ΔT_s on a 10 ms time scale as the cyclotron energy is deposited isotropically as heat in the plasma, through ion-ion collisions.

We find $\Delta T_s \propto (\delta_s/M_s)(A_B \tau_B)^2$ for short bursts $\tau_B \lesssim 0.1$ ms, as shown in Fig. 3.3. Here the center-of-mass mode of $^{24}\mathrm{Mg}^+$ and $^{26}\mathrm{Mg}^+$ are excited at $f_1^{(24)} = 1894.6$ kHz and $f_1^{(26)} = 1745.2$ kHz, with short bursts of 100 and 200 cycles. The amount of heating is dependent on the concentration of the species δ_s, with the majority species $^{24}\mathrm{Mg}^+$ heating the plasma about 4× more than the minority species

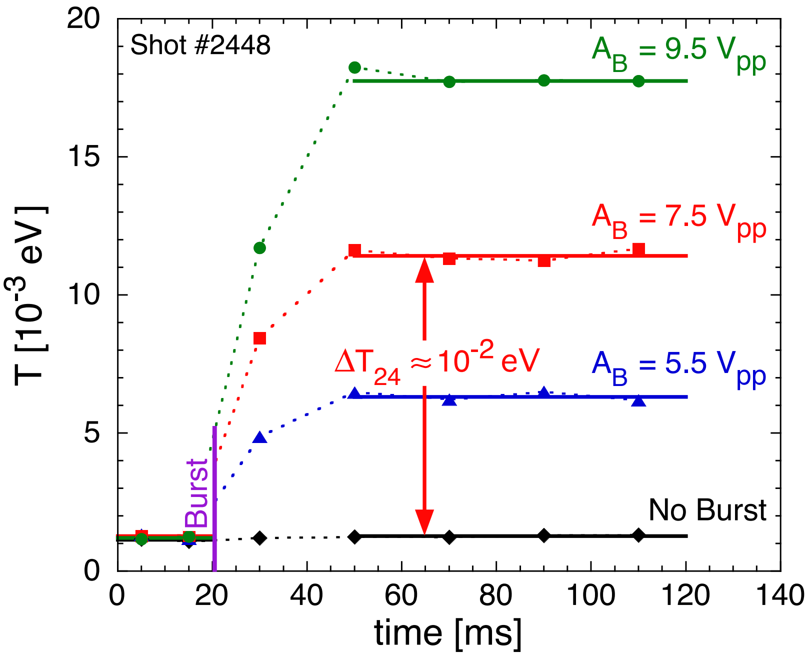

Figure 3.2: Time evolution of the plasma temperature after the excitation of the center-of-mass mode of $^{24}\text{Mg}^+$ at three different burst amplitudes A_B. A 200 cycle RF burst at $f_1^{(24)} = 1894.6$ kHz is used, corresponding to a short burst period $\tau_B = 0.1$ ms.

$^{26}\text{Mg}^+$.

This ΔT_s scaling is consistent with a center-of-mass model. Consider an ion initially at rest in the plasma, which is then excited at the species center-of-mass cyclotron frequency $\omega_1^{(s)} = 2\pi f_1^{(s)}$ by a sinusoidal electric field of amplitude E_0. The resulting motion can be model as an undamped driven harmonic oscillator,

$$\ddot{r} + \left[\omega_1^{(s)}\right]^2 r = \frac{q_s E_0}{M_s} \sin\left[\omega_1^{(s)} t\right]. \tag{3.1}$$

The amplitude of the driven cyclotron motion increases linearly in time, with an average energy in an oscillation of

$$\langle \mathcal{E}_s \rangle \propto \frac{q_s^2}{M_s} (A_B \tau_B)^2, \tag{3.2}$$

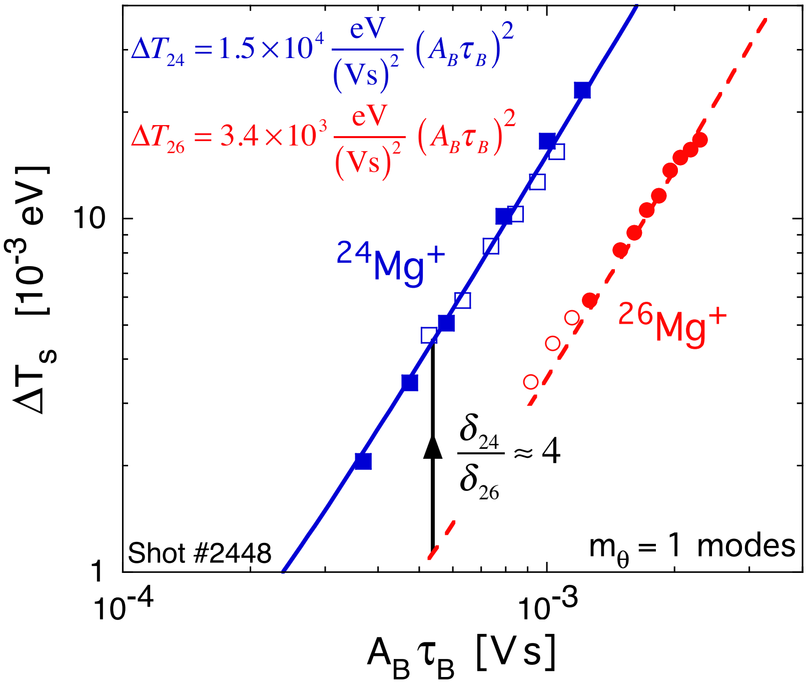

Figure 3.3: Change in the plasma temperature versus burst amplitude A_B and burst period τ_B for the majority species ^{24}Mg$^+$ and a minority species ^{26}Mg$^+$. Open and closed symbols correspond to bursts consisting of 100 and 200 cycles respectively.

neglecting smaller terms linear in the burst period. The strength of the electric E_0 is proportional to the burst amplitude A_B applied to the azimuthally sectored confinement ring.

A plasma consisting of $\delta_s N_{tot}$ identical ions, each excited by a resonant cyclotron burst to an energy $\langle \mathcal{E}_s \rangle$, will heat the plasma by $\Delta T_s \propto \delta_s (A_B \tau_B)^2 / M_s$. This model is in agreement with the measurements shown in Fig. 3.3. From the $(A_B\tau_B)^2$ fits, we calculate the relative concentration of the Mg$^+$ isotopes $\delta_{26}/\delta_{24} = (M_{26}/M_{24})(\Delta T_{26}/\Delta T_{24})$, which is within 10% of those obtained from LIF diagnostics. Thus, the plasma heating from short resonant bursts enables quantitative measurements of the relative species fractions.

This model has ignored any dephasing between the oscillator and the drive, which can result from collisions, damping, or an initially off-resonant burst. Dephasing will result in less energy per ion, and a smaller ΔT_s. We find that the $\Delta T_s \propto (A_B \tau_B)^2$ scaling is only valid for short bursts $\tau_B \lesssim 0.1$ ms. As the burst period is increased, keeping $A_B \tau_B$ constant, we observe a decrease in the plasma heating. At a $\tau_B \sim 1.7$ ms ($\sim$ 3000 cycles), the heating is decreased to less than 40% of the short burst expectation, with a larger decrease for the minority species.

This dephasing for long bursts explains why the height of the peaks in Fig. 3.1 underestimate the concentrations of the minority species. At present it is unclear what is causing the dephasing on this time scale. We have changed the initial plasma temperature by an order of magnitude $(10^{-3} \rightarrow 10^{-2})$ eV to no effect, and the burst frequency is accurate to a few hundred Hz, ruling out an off-resonant drive.

3.4 Radially Uniform Plasma

Frequency shifts are measured for the $m_\theta = 0$, 1, and 2 cyclotron modes having density perturbations on the plasma radial surface varying as $\delta n \propto \cos(m_\theta \theta - 2\pi f_{m_\theta}^{(s)} t)$, as shown in Fig. 3.4. For the $m_\theta = 1$ mode, the ion orbits are in phase, resulting in a displacement of the center-of-mass of the exited species, which then orbits the center of the trap at $f_1^{(s)}$, as in Fig. 3.4 (a). This mode is excited by a dipole burst on an azimuthally sectored confinement ring. A quadrupole burst can excite the "elliptical", $m_\theta = 2$ mode [32, 7]. As shown in Fig. 3.4 (b), this elliptical density perturbation, rotating at $f_2^{(s)}$, is created by a 180° phase shift of the ion orbits on opposite radial edges of the plasma. The final mode we have analyzed is the novel $m_\theta = 0$, radial "breathing" mode [33, 34, 35] in which the plasma cross-section expands and contracts radially, as shown in Fig. 3.4 (c). To excite this mode, the end of the plasma is wiggled

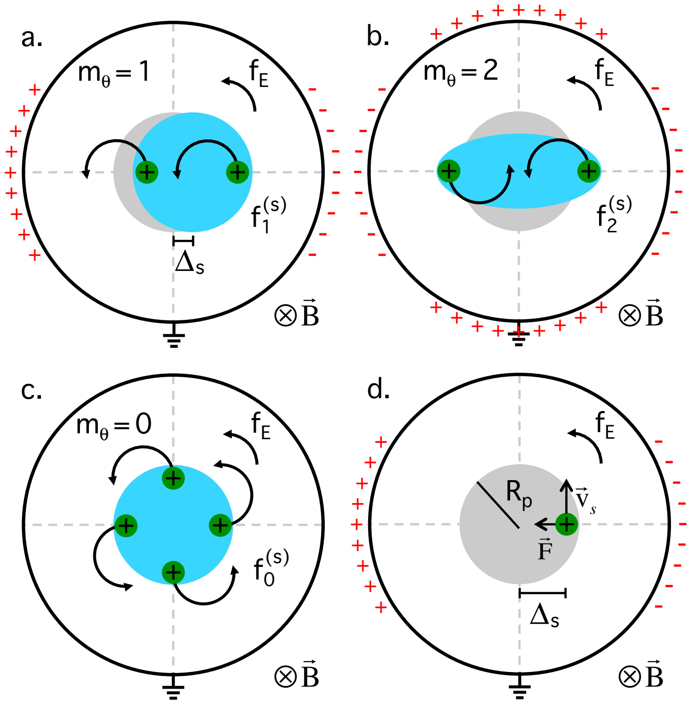

Figure 3.4: Sketches of the $m_\theta = 1$, 2, and 0 surface waves (a-c); and simple clump model (d). The cyclotron mode frequencies are shifted proportional to the $E \times B$ drift-rotation frequency f_E arising from the *non-resonant* species, image charges on the trap wall, and trap potentials.

at $f_0^{(s)}$, because the wave generates no external electric field except at the plasma end. The ion orbits are typically excited to twice the thermal cyclotron radius, which at $T \sim 10^{-2}$ eV is about 40 μm.

Figure 3.5 shows the $m_\theta = 0, 1,$ and 2 cyclotron mode frequencies for $^{24}\mathrm{Mg}^+$. The $m_\theta = 0$ and $m_\theta = 1$ modes are downshifted from the "bare" cyclotron frequency $F_c^{(24)} = 1899.46$ kHz, while the $m_\theta = 2$ mode is upshifted. The cyclotron mode frequencies are measured from the peaks in this heating response, with an accuracy of approximately 100 Hz. The difference in frequency between each pair of adjacent modes closely equals the measured $E \times B$ rotation frequency $f_E = 9.3$ kHz. We note that the width of these resonances is a possible measurement of the mode damping γ.

In the case of the $m_\theta = 1$ mode, this downshift away from the "bare" cyclotron

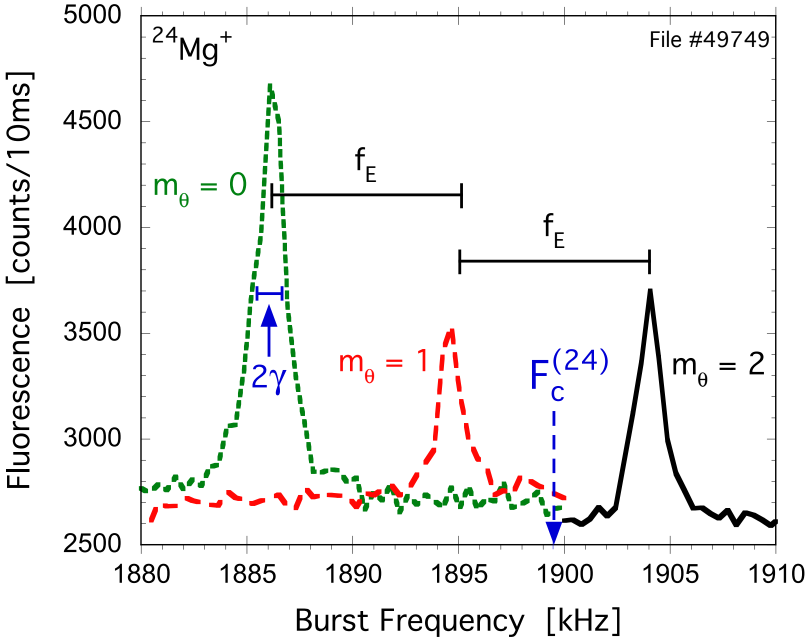

Figure 3.5: Observed ^{24}Mg$^+$ cyclotron resonances for $m_\theta = 0$, 1, and 2 modes. Modes are shifted away from the "bare" cyclotron frequency $F_c^{(24)} = 1899.46$ kHz. These modes have a frequency spacing of approximately the $E \times B$ rotation frequency $f_E = 9.3$ kHz.

frequency can be understood through a simple "clump" model. Sketched in Fig. 3.4 (d) is a cylindrical trap confining a multi-species ion plasma. A species is excited to an amplitude Δ_s, and undergoes uniform circular motion about the center of the trap with a velocity v_s, resulting in a frequency $f_1^{(s)} = \mathrm{v}_s/2\pi\Delta_s$. The dynamics of this excited species can be modeled by a point particle located at the center-of-mass of the excited species. The radial forces acting on this point particle are the centrifugal, $\mathrm{v}_s \times B$, and electrostatic forces, summing to zero as

$$\frac{M_s \mathrm{v}_s^2}{\Delta_s} - \frac{q_s}{c}\mathrm{v}_s B_z + q_s \tilde{E}_r = 0. \tag{3.3}$$

Here $\tilde{E}_r$ represents the electric field generated by the *non-resonant* species, trap potentials, and image charge on the trap wall; rather than the total electric field

E_r measured through f_E. (That is, the clump cannot push on itself.) Equation 3.3 reduces to $f_1^{(s)} = F_c^{(s)}$ when $\tilde{E}_r = 0$. However, $\tilde{E}_r > 0$ increases the outward radial force, mandating a downshift in the center-of-mass mode frequency.

In these experiments, the radial electric field $\tilde{E}_r$ is controlled by compressing the plasma with the RW, and the strength of this electric field is measured through the $E \times B$ rotation frequency f_E. In Fig. 3.6, the measured cyclotron modes frequencies of the $m_\theta = 0$, 1, and 2 modes are plotted versus f_E for the majority species $^{24}\mathrm{Mg}^+$ and minority species $^{25}\mathrm{Mg}^+$ and $^{26}\mathrm{Mg}^+$. The cyclotron mode frequency shifts are proportional to f_E, but the proportionality constants are different for the majority species $^{24}\mathrm{Mg}^+$ than for the minority species $^{25}\mathrm{Mg}^+$ and $^{26}\mathrm{Mg}^+$, due to collective plasma effects.

These cyclotron mode frequencies including collective effects can be obtained from surface wave theory. This theory assumes a cold, radially unform plasma of infinite length, and solves the Vlasov-Poisson equation for a $\cos(m_\theta \theta)$ surface perturbation in a frame rotating with the plasma at f_E. Frequency shifts of the form

$$f_{m_\theta}^{(s)} - F_c^{(s)} = \left[(m_\theta - 2) + \delta_s(1 - \mathcal{R}_{m_\theta})\right] f_E, \tag{3.4}$$

are predicted [30, 31, 4]. The $\delta_s(1 - \mathcal{R}_{m_\theta}) f_E$ term represents collective interactions in the plasma frame rotating at f_E; the $-2f_E$ term is a shift due to the Coriolis force in the plasma frame; and the $m_\theta f_E$ term is the Doppler shift back to the lab frame. For $m_\theta \geq 1$, the wall image charge correction is $\mathcal{R}_{m_\theta} \equiv (R_p/R_w)^{2m_\theta}$, but $\mathcal{R}_{m_\theta} \equiv 0$ for $m_\theta = 0$.

For the $m_\theta = 1$ mode, surface wave theory predicts a frequency shift of $(\delta_s - 1) f_E - \delta_s (R_p/R_w)^2 f_E$. This frequency shift can be interpreted from the simple

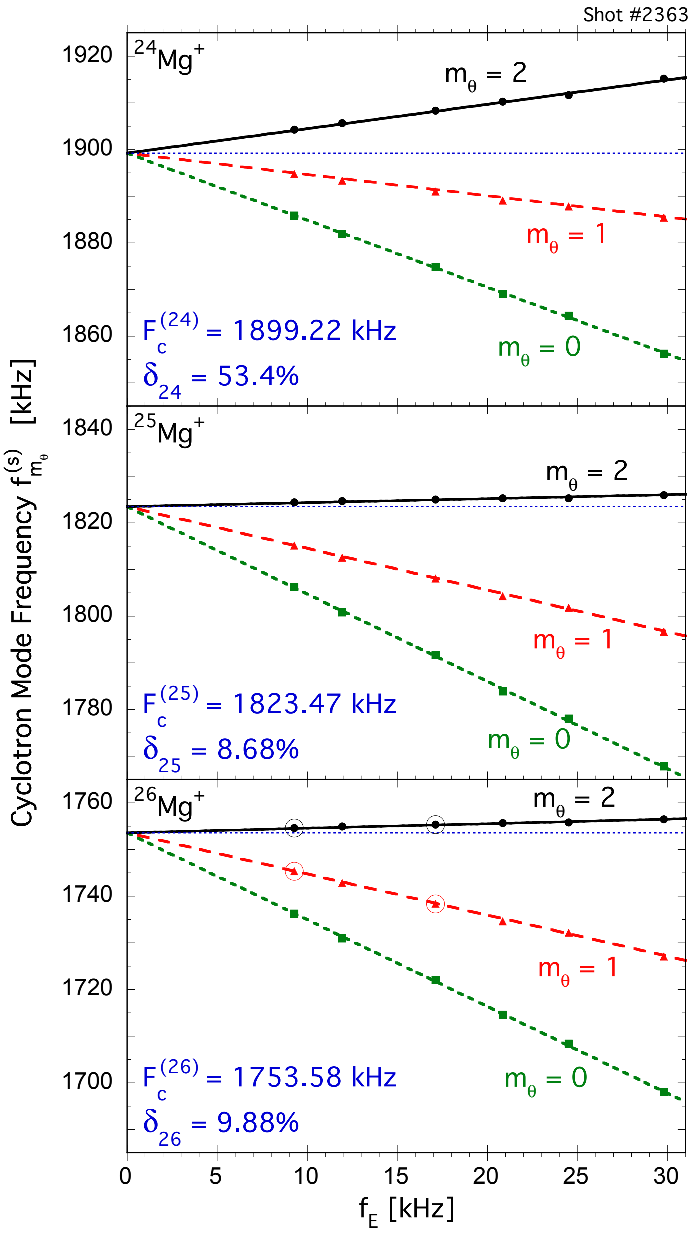

Figure 3.6: Cyclotron mode frequencies versus measured f_E for ^{24}Mg^{+}, ^{25}Mg^{+}, and ^{26}Mg^{+}. Symbols are experimental data and curves are fits to Eq. 3.4, which determine $F_c^{(s)}$ (dotted) and δ_s for each species.

clump model. The $(\delta_s - 1)f_E$ term represents the radial electric field from the *non-resonant* species. A species clump cannot exert a force on itself, reducing the effective space charge electric field by δ_s. However, the image charges of the clump *do* exert a force on the clump center-of-mass, represented here by a frequency shift of

$$f_D^{(s)} = \delta_s f_E \left(\frac{R_p}{R_w} \right)^2 , \tag{3.5}$$

equal to the species $m_\theta = 1$ diocotron frequency. In these experiments $R_p << R_w$, so the dominant frequency shift is caused by the *non-resonant* species. The image charge frequency shift $f_D^{(s)} < 200$ Hz, and is dependent on the concentration of the species.

Fitting Eq. 3.4 to the measured frequency shifts in Fig. 3.6, we find that the observed mode frequency spacing is consistent to within the 2% accuracy of the LIF measurements of f_E, and that these cyclotron modes converge to the "bare" cyclotron frequency $F_c^{(s)}$ in the limit $f_E \to 0$. Also, the slope of the frequency shifts in Fig. 3.6 provide a measurement of the species fractions δ_s for each species. The relative Mg^+ ratios δ_{25}/δ_{24} and δ_{26}/δ_{24} are within 20% of those obtained through LIF diagnostics, and within 5% of that obtained from the resonant wave absorption technique. The corresponding mass ratios from $F_c^{(s)}$ are accurate to within 200 ppm.

Four frequencies $f_{m_\theta}^{(s)}$ from two m_θ modes in two plasma states could be used to determine the plasma characteristics f_E and δ_s, and thereby determine $F_c^{(s)}$. In Fig. 3.6, the measured cyclotron frequency differences of the two circled (vertical) data pairs give $f_E = (9.33, 16.97)$ kHz versus the measured $(9.29, 17.13)$ kHz; and Eq. 3.4 then gives $\delta_{26} = 9.06\%$ and $F_c^{(26)} = 1753.82$ kHz, in close agreement with the results in Fig. 3.6. Of course, similar information from multiple species would improve this plasma characterization.

This surface wave theory [30, 31, 4] has ignored finite-length effects resulting from the trap end potentials. These effects have been measured on the low-frequency diocotron mode in electron plasmas [36]. Extending these results to the plasma conditions of our experiments, we find that finite-length effects produce a frequency shift of approximately 50 Hz.

In a single species plasma ($\delta = 1$), the frequency shifts from trap potentials and image charge are dominant, because there are no *non-resonant* species. Prior work [32] measured the center-of-mass cyclotron mode frequency on electron plasmas, and found that the $m_\theta = 1$ mode is downshifted by the diocotron frequency f_D due to image charge in the conducting walls. Later multi-species work [7] described the spacing between the m_θ-modes in terms of several f_D when image charges dominated. This prior work was conducted on hot plasmas $T \sim 3$ eV, with parabolic density profiles extending to large R_p/R_w. In general, f_E is the more fundamental parameter describing these frequency shifts, since image charge forces are generally weak.

3.5 Mass Spectroscopy Calibration Equation

The accuracy of Fourier transform ion cyclotron resonance mass spectrometry (FTICR-MS) is often limited by these cyclotron frequency shifts. Conversion from the measured cyclotron frequency to a mass to charge ratio $(M/q)_s$ is typically done using one of the several calibration equations [10], which correct for the space charge electric field and its influence on the cyclotron frequency. In this section, we extend the simple clump model to calculate a calibration equation consistent with our experimental results.

Solving for $(M/q)_s$ in Eq. 3.3 produces a calibration equation,

$$\left(\frac{M}{q}\right)_s = \frac{B_z}{2\pi c f_1^{(s)}} - \frac{1}{(2\pi f_1^{(s)})^2} \frac{\tilde{E}_r}{\Delta_s}. \tag{3.6}$$

The accuracy of Eq. 3.6 depends on correctly modeling $\tilde{E}_r/\Delta_s$ at the radial position Δ_s of the clump. Note that E_r/r represents the $E \times B$ drift rotation frequency as $f_E(r) = (cE_r/r)/2\pi B$. In our experiments, f_E is uniform with r.

When the equilibrium charge densities are uniform and the excitation amplitude is small (i.e., $\Delta_s < R_p$), the electric field ratio $\tilde{E}_r/\Delta_s$ is basically independent of radius. Then, the "calibration" of Eq. 3.6 is independent of radius. The ion cloud is also assumed to be long compared to its radius $L_p >> R_p$, so that the ion cloud and image charge electric fields can be approximated as those of an infinitely long cylinder. The partial electric field $\tilde{E}_r$ produced from the non-excited ion cloud species, from image charges of the excited species, and from trap potentials V_T is then

$$\frac{\tilde{E}_r}{\Delta_s} = 2\pi(1-\delta_s)en_0 + 2\pi\delta_s en_0 \mathcal{R}_1 + 2V_T G_T, \tag{3.7}$$

where $en_0 = Q_0/\pi R_p^2 L_p$ is the total charge density, and G_T is a trap-dependent geometrical factor relating the z-averaged E_r/r to the applied V_T [37].

Here we see that the dependence on δ_s comes from the reduction of the effective electric field, since the excited species clump cannot apply a force on itself; and from the image charge in the confining wall, which does apply a force on the excited clump. The image charges of the non-excited species are θ-symmetric, and the image charges of any other excited species are assumed to be non-resonant and therefore time-average to zero. By taking $\delta_s \to 0$ (i.e., treating a single particle excitation and ignoring image charge), this electric field $\tilde{E}_r$ reduces to that of Jeffries et al. [37].

From this $\tilde{E}_r/\Delta_s$, a calibration equation can be obtained,

$$\left(\frac{M}{q}\right)_s = \frac{\overbrace{B_z}^{A}}{2\pi c}\frac{1}{f_1^{(s)}} + \left[\overbrace{-\left(\frac{2\pi e n_0 + 2V_T G_T}{(2\pi)^2}\right)}^{B} + \overbrace{e n_0 \left\{\frac{1-\mathcal{R}_1}{2\pi}\right\}}^{C}\delta_s\right]\frac{1}{(f_1^{(s)})^2}. \tag{3.8}$$

This calibration equation depends on the relative charge density δ_s of species s. If the excitation amplitudes Δ_s are the same for each species, then the received wall signal I_s is a measure of δ_s, and Eq. 3.8 results in the "intensity-dependent" calibration equation of Refs [38, 27]. In general, I_s is only an approximate measure of δ_s because it is also proportional to the excitation amplitude as $I_s \propto \delta_s\Delta_s$. The parameters A and B are identical to those of the simplest calibration equation in general use [29]. They calibrate single particle effects such as the magnetic field strength, and frequency shifts from the entire ion cloud and trap potentials. Parameter C corrects for overestimating the frequency shift from the ion cloud when self forces between the excited species and itself were included, and also includes the effects of image charge.

3.6 Non-Uniform Species Fractions

In this section, we investigate the cyclotron mode frequencies on plasmas with radially non-uniform species fractions $n_s(r)$. The radial distribution of each species varies because of centrifugal mass separation. When uniformly distributed, species of different mass drift-rotate at slightly different rates, and therefore experience viscous drags in the azimuthal direction. These drags produces $F_{drag} \times B_z$ radial drifts, which radially separate each species and forms a more uniform rotation profile. The species concentrate into separate radial annuli, each approaching the full plasma density n_0, with the lighter species on center.

The equilibrium density profiles of each species can be theoretically determined. The ratio of densities between two species is equal to

$$\frac{n_a(r)}{n_b(r)} = C_{ab} \exp\left[\frac{1}{2T}(M_a - M_b)(2\pi f_E)^2 r^2\right], \tag{3.9}$$

where C_{ab} is a constant determined by the overall fraction of each species [20]. The effects of centrifugal mass separation are important for species with a large mass difference and for cold plasmas.

Shown in Fig. 3.7 are measured density profiles for both a warm plasma with minimal separation, and a cold plasma with strong separation. The symbols represent the LIF measured densities of the Mg^+ isotopes, and the solid black line is the total plasma density n_0 measured through the $E \times B$ rotation frequency. The curves are theory predicted profiles for the measured species fractions δ_s, plasma rotation frequency f_E, and "top-hat" radius R_p. These theory profiles have been convolved with the finite size probe laser beam σ_L, so they can be compared directly with the experimental measurements.

At $T = 4.8 \times 10^{-3}$ eV, the species are uniformly mixed, as shown in Fig. 3.7 (Top). This is a typical example of a radially uniform plasma. Here the species fractions $\delta_s \equiv n_s/n_0$ are constant over the plasma radius, and the cyclotron mode frequencies are well described by Eq. 3.4. Note that the sum of the Mg^+ isotopes is not equal to the total plasma density due to the presence of impurity ions, $\mathrm{H_3O}^+$ and O_2^+, not detected by the LIF diagnostics.

As the plasma is cooled, the species centrifugally separate and concentrate into radial annuli increasing the "local" $n_s(r)$. At $T = 7.1 \times 10^{-5}$ eV, the $^{24}\mathrm{Mg}^+$ has

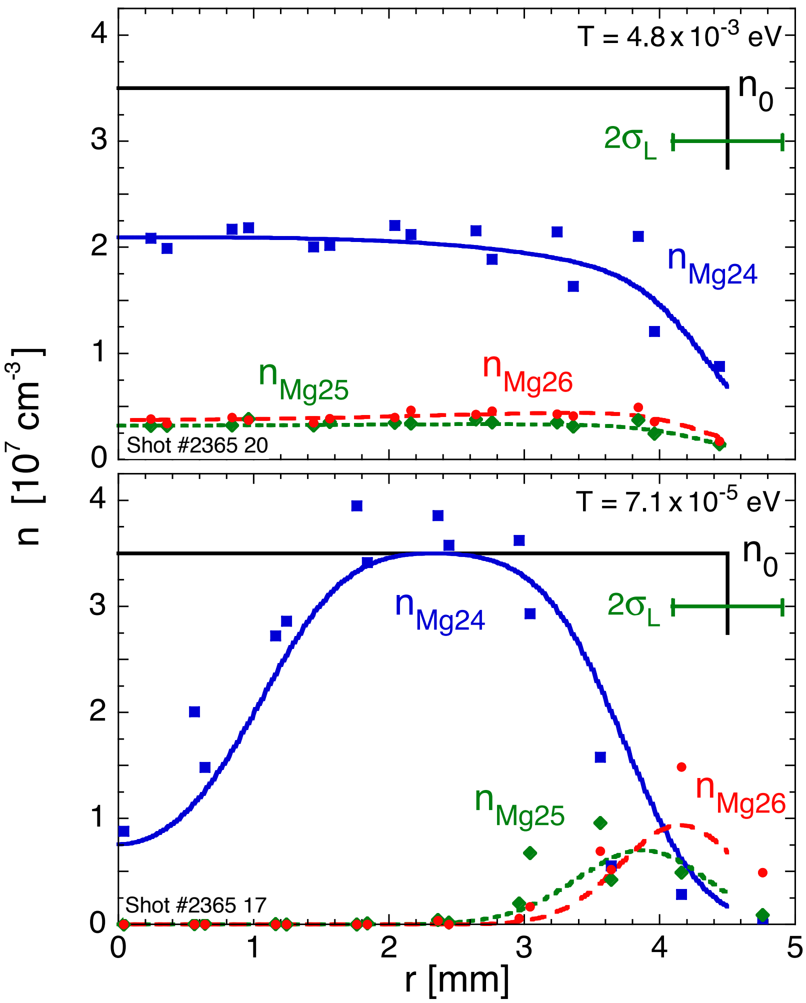

Figure 3.7: Radial density profiles of both a warm (Top) and a cold (Bottom) plasma. Symbols are the measured laser-width averaged data, and solid black lines represent the total plasma density n_0 measured through f_E. The curves are theory predicted profiles resulting from Eq. 3.9, with measured $f_E = 17.0$ kHz, $R_p = 4.5$ mm, $M_s = (24, 25, 26, 19, 32)$ amu, and $\delta_s = (54, 9, 12, 8, 17)\%$.

approached the full plasma density n_0, pushing the heavier Mg^+ isotopes to the radial edge, as shown in Fig. 3.7 (Bottom). The central hole observed in the Mg^+ density profile is a result of the lighter impurity species $\mathrm{H_3O}^+$. Although the radially-averaged species fractions are unchanged, the peak "local" fractions $\delta_s(r) \equiv n_s(r)/n_0$ have increased for each species. We find that the cyclotron mode frequencies are dependent on these peak "local" species fractions.

Shown in Fig. 3.8 are measurements of the $m_\theta = 1$ frequency shifts as the "local" species concentrations are varied by altering the plasma temperature. These shifts are measured on $^{24}\mathrm{Mg}^+$, $^{26}\mathrm{Mg}^+$, and $\mathrm{H_3O}^+$. At $T \gtrsim 10^{-3}$ eV, the species are uniformly mixed and the frequency shifts are approximately $(\delta_s - 1)f_E$, as predicted by Eq. 3.4. Cooling the plasma increases the "local" species concentrations, and decreases the $m_\theta = 1$ frequency shift. At the coldest temperatures $T \sim 10^{-4}$ eV, the "local" $^{24}\mathrm{Mg}^+$ and $\mathrm{H_3O}^+$ densities have approached the full plasma density n_0, and the center-of-mass cyclotron mode frequency is nearly the "bare" cyclotron frequency. Similar frequency shifts are observed for both the $m_\theta = 0$ and $m_\theta = 2$ modes, offset by $(m_\theta - 1)f_E$.

The full cyclotron mode analysis was developed by Dubin in Ref. [31]. For radially varying ion densities $n_s(r)$ or varying rotation $f_E(r)$, the mode resonances at $f^{(s)}_{m_\theta}$ are predicted by peaks in the real part of the admittance $Re(Y_{m_\theta})$. Here $Y_{m_\theta} \equiv I/V$ relates electrode displacement current I to electrode voltage V. It has a frequency dependence of

$$Y_{m_\theta} \propto i(2\pi f)\frac{G_{m_\theta} + 1}{G_{m_\theta} - 1}, \tag{3.10}$$

with

$$G_{m_\theta} \equiv -\frac{2m_\theta}{R_w^{2m_\theta}} \int_0^{R_w} dr\, \frac{\beta(r)\, r^{2m_\theta - 1}}{\alpha(r) - \beta(r)}, \tag{3.11}$$

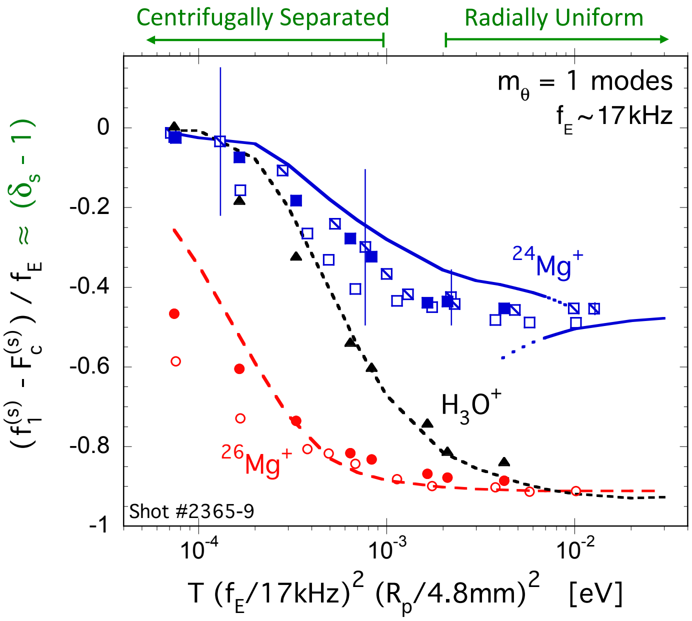

Figure 3.8: Normalized shifts of the $m_\theta = 1$ cyclotron mode frequencies for $^{24}\mathrm{Mg}^+$, $^{26}\mathrm{Mg}^+$, and $\mathrm{H_3O}^+$, as the "local" species concentrations increase due to centrifugal separation. Symbol shapes represent species; symbol fill distinguishes measurements on three plasmas with slightly different compositions. The temperature T is scaled by the centrifugal energy of these plasmas, which differ by approximately 25%. Curves are theory predictions assuming a typical species concentration $M_s = (24, 25, 26, 19, 32)$ amu with $\delta_s = (54, 9, 9, 8, 20)\%$. The four vertical lines are the FWHM of the $^{24}\mathrm{Mg}^+$ cyclotron resonance at various temperatures.

$$\beta(r) \equiv \frac{n_s(r)}{n_0} f_E(0), \tag{3.12}$$

and

$$\alpha(r) \equiv (f_{m_\theta}^{(s)} - F_c^{(s)} + i\gamma/2\pi) - (m_\theta - 2) f_E(r) + \frac{r}{2}\frac{\partial}{\partial r} f_E(r). \tag{3.13}$$

Peaks in $Re(Y_{m_\theta})$ occur when $G_{m_\theta} \rightarrow 1$.

The curves in Fig. 3.8 are the shifts resulting from numerically integrating Eq. 3.10 with $n_s(r)$ as predicted for centrifugal separation, Eq. 3.9. As the plasma is cooled, the "local" $n_s(r)$ increases towards the full "top-hat" density n_0: this isolates the species, and removes frequency shifts from the electric field of other species. As a result, the cyclotron mode frequencies are shifted towards the single-species $\delta_s = 1$ limit with ordinate 0. Here, the remaining shifts due to image charge [31] and trap electric fields are negligible. The discontinuity in the $^{24}\mathrm{Mg}^+$ theory curve is due to multiple modes with different radial mode structure. Although multiple radial modes have been observed on some plasmas they were not observed for this set of data possibly due to stronger damping.

Varying the plasma temperature also changes the observed width of the cyclotron resonance as shown by the four vertical FWHM (2γ) bars in Fig. 3.8. At high temperatures $T \gtrsim 10^{-2}$ eV, the observed resonance width is determined by the frequency width of the drive, which is approximately 0.4 kHz. When the plasma is cooled, the ion-ion collision frequency $\nu_{\perp\|}$ increases, and the observed resonance width probably reflects collisional damping of the cyclotron modes, varying qualitatively like $\nu_{\perp\|}$. For $T \lesssim 10^{-3}$ eV, inter-species collisions are reduced by centrifugal separation of the species, and the cyclotron resonance width is observed to remain constant at approximately 6 kHz.

3.7 Bernstein Waves

At temperatures $T \gtrsim 0.1$ eV, where ion-ion collisionality is small, we observed multiple closely-spaced modes near F_c with spacing dependent on T. This mode splitting is similar to that observed in electron plasmas [32]; but here this splitting occurs for the $m_\theta = 1$ mode where no splitting was previously seen. Theory work in progress analyzes radially standing Bernstein waves in multi-species ion plasmas [31], and a connection to this theory is being pursued.

3.8 Conclusion

On radially uniform plasmas, the $m_\theta = 0$, 1, and 2 cyclotron mode frequencies are shifted by radial electric fields and collective effects in agreement with surface wave theory, Eq. 3.4. These frequency shifts can be used to measure the plasma $E \times B$ rotation frequency f_E, and species fractions δ_s. This quantitative understanding of the frequency shifts give a physical basis for the "space charge" and "amplitude" calibration equations commonly used in mass spectroscopy. For short bursts $\tau_B \lesssim 0.1$ ms, the plasma heating from resonant wave absorption of the $m_\theta = 1$ mode is found to be $\Delta T_s \propto \delta_s (A_B \tau_B)^2 / M_s$, providing another diagnostic tool of δ_s. For non-uniform plasmas, the cyclotron mode frequencies are dependent on the "local" species concentrations, and the frequency shifts from *non-resonant* species are removed when the excited species is completely separated.

3.9 Acknowledgements

This chapter, in part, is a reprint of the material as it appears in three journal articles: M. Affolter, F. Anderegg, D. H. E. Dubin, and C. F. Driscoll, *Physics Letters A*, **378**, 2406 (2014); M. Affolter, F. Anderegg, D.H.E. Dubin and C.F. Driscoll, *Physics of Plasmas*, **22**, 055701 (2015); and M. Affolter, F. Anderegg, C.F. Driscoll, *Journal of the American Society for Mass Spectrometry*, **26**, 330 (2015). The dissertation author was the primary investigator and author of these papers.

Chapter 4

Inter-species Drag Damping of Langmuir Waves

4.1 Introduction

Collision rates are fundamental to our understanding of transport phenomena in plasmas. In magnetized plasmas, the cyclotron radius r_c is often less than the Debye length λ_D, and classical 3D Boltzmann collisions are limited to short-range, with impact parameters $\rho < r_c$. Rarely considered in these magnetized plasmas are long-range ($r_c < \rho < \lambda_D$) collisions described by guiding centers interacting as they move along the magnetic field. However, experiments and theory have shown that these long-range collisions can enhance cross-field diffusion [39, 40], heat transport [41, 42], and viscosity [43, 44] by orders of magnitude in regimes where $\lambda_D > r_c$.

Recent theory [12] provides a precise analysis of these long-range collisions on the parallel slowing rate in a magnetized plasma. A new fundamental length scale d was identified, separating collisions into regimes: $\rho < d$ where the colliding particles can be treated as two-body, point-like Boltzmann collisions; and $\rho > d$ a Fokker-Planck regime where multiple weak collisions occur simultaneously. This theory predicts that the rate of collisional slowing parallel to the magnetic field is strongly enhanced by long-range collisions. This enhancement of the parallel slowing rate applies to Penning trap plasmas for both matter and antimatter [45, 46, 47], for some astrophysical plasmas [48], and even for the edge region of tokomak plasmas [49, 50, 51].

Here we present the first experimental confirmation of this enhanced collisional slowing rate, obtained through measurements of the damping of Langmuir waves in a multi-species ion plasma. Collisional drag damping theory predicts damping proportional to the collisional slowing rate. The measured damping rates are in quantitative agreement with the theory when long-range collisions are included: exceeding predictions considering only 3D Boltzmann, short-range collisions by as much as an order of magnitude.

These measurements of collisional drag damping extend over a range of two decades in temperature. When collisions are weak and the ion species are uniformly mixed, the damping rates are proportional to the collisionality, scaling roughly as $T^{-3/2}$. The damping is reduced at low temperatures as centrifugal mass separation (see Sec. 3.6) and collisional locking of the fluid elements becomes significant. At ultra-low temperatures, the plasma approaches the moderately correlated regime, and these damping measurements may provide insight into the collisionality of a correlated, magnetized plasma.

4.2 Species Concentrations

As discussed in Sec. 3.3, a quantitative determination of the species fractions δ_s can be obtained by measuring the resulting heating from short, resonant cyclotron bursts. The species fractions are measured to a 10% accuracy down to a $\delta_s \sim 0.5\%$ level. The plasma composition are varied by changing the background gas pressure. Table 4.1 shows the five different plasma compositions discussed in this chapter.

Table 4.1: Inter-species drag damping has been investigated on five plasmas with different species compositions as listed in this table. The compositions were controlled by varying the background gas pressure.

Species	$^{24}Mg^+$	$^{25}Mg^+$	$^{26}Mg^+$	H_3O^+	HCO^+	O_2^+	$C_3H_3^+$	$C_3H_7^+$
Mass [amu]	24	25	26	19	29	32	39	43
dirty [%]	52	9	10	16	4	4	4	1
semi-dirty [%]	64	12	11	10	2	1		
clean [%]	63	14	18	~2-5				
high density [%]	53	8	8	19	5	5	2	
low density [%]	52	5	4	24		12	3	

4.3 Trivelpiece-Gould Waves

The measurements of collisional drag damping are preformed on Langmuir waves. In these bounded plasmas, the Langmuir waves are near-acoustic with $\omega \propto k$, because of the shielding of the cylindrical confinement electrodes at a radius $R_w = 2.86$ cm. This Trivelpiece-Gould (TG) dispersion relation [52, 53] for azimuthally symmetric modes is approximately

$$f_{TG} = f_p \frac{k_z}{\sqrt{k_z^2 + k_\perp^2}} \left[1 + \frac{3}{2} \left(\frac{\bar{\mathrm{v}}}{\mathrm{v}_{ph}} \right)^2 \right], \tag{4.1}$$

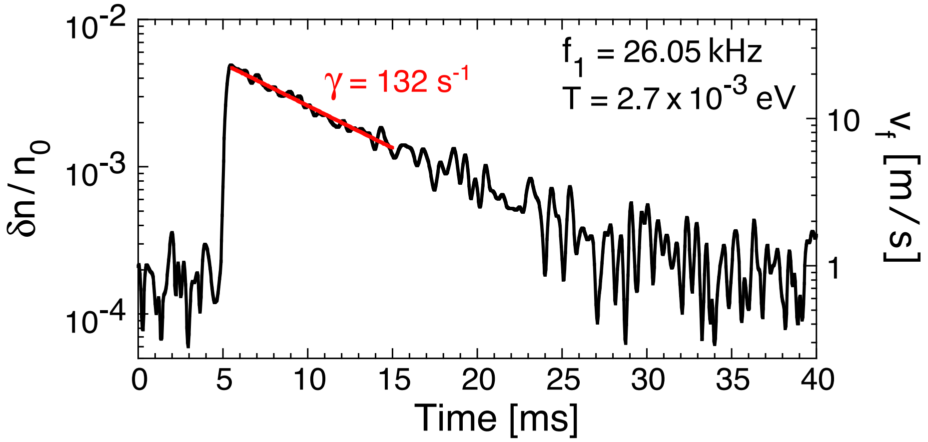

Figure 4.1: The amplitude evolution of an $m_z = 1$ TG wave. An exponential fit (red curve) to the decreasing amplitude determines the damping rate. The measured mode frequency remains constant over the evolution.

where $k_z \equiv m_z\pi/L_p$ and $k_\perp = R_p^{-1}[2/\ln(R_w/R_p)]^{1/2}$ are the axial and transverse wavenumbers respectively, and f_p is the plasma frequency.

Here, these TG waves are excited with a burst near the linear mode frequency applied to an end confinement ring, and detected on a confinement ring located near the plasma center. Typically, a 10 cycle sine wave burst with a 5 mV_{pp} amplitude is used, resulting in a wave density perturbation $\delta n/n_0 \sim 0.5\%$, wave fluid velocity $\text{v}_f \sim 20$ m/s, and a concomitant heating of the plasma by about 3×10^{-5} eV. For most of this work, we investigate the damping of the lowest order $m_z = 1$ axial mode occurring at a frequency $f_1 \sim 26$ kHz.

The time evolution of the wave amplitude, as shown in Fig. 4.1, is obtained through sine wave fits to the detected signal in time segments of approximately 5 wave cycles. An exponential fit to this decreasing wave amplitude determines the damping rate γ. At $T = 2.7 \times 10^{-3}$ eV, a typical damping rate is $\gamma \sim 132$ s^{-1} for a “dirty” plasma composition.

4.4 Damping Measurements

Figure 4.2 shows measurements of the damping rate over four decades in the plasma temperature. At high temperatures ($T \sim 0.5$ eV), collisionless Landau damping dominates. Quantitative agreement with Landau theory is obtained for small amplitude waves as indicated by the solid red curve [11]. This prototypical Landau damping becomes exponentially weak for $T \lesssim 0.2$ eV. However, we believe the damping in the regime $0.02 \lesssim T \lesssim 0.2$ eV is a result of the same Landau interaction, but on "bounce-harmonics" of the wave, caused by finite-length effects. Recent experiments [54] conducted in this temperature regime have demonstrated that an externally applied "squeeze" increases these wave harmonics, causing stronger damping in quantitative agreement with recent bounce harmonic Landau damping theory [55].

At cryogenic temperatures ($T \lesssim 10^{-2}$ eV), the damping is proportional to the collisionality: dependent on the plasma composition and scaling roughly as $T^{-3/2}$. Figure 4.2 shows damping measurements on plasmas with three different compositions as listed in Table 4.1. Short cyclotron bursts were used to measure the "dirty" and "semi-dirty" plasma compositions; whereas, the "clean" composition is an estimate from the size of the H_3O^+ hole in a centrifugally separated Mg^+ density profile, similar to Fig. 3.7. We find that the damping increases by a factor of 4 as the concentration of impurities is increased from the "clean" to "dirty" plasma compositions. For $T \lesssim 10^{-3}$ eV, the damping is observed to decrease from the $T^{-3/2}$ scaling consistent with the onset of centrifugal mass separation. The fact that the measured damping is dependent on the plasma composition and scales as $T^{-3/2}$ suggests inter-species drag as the observed damping mechanism.

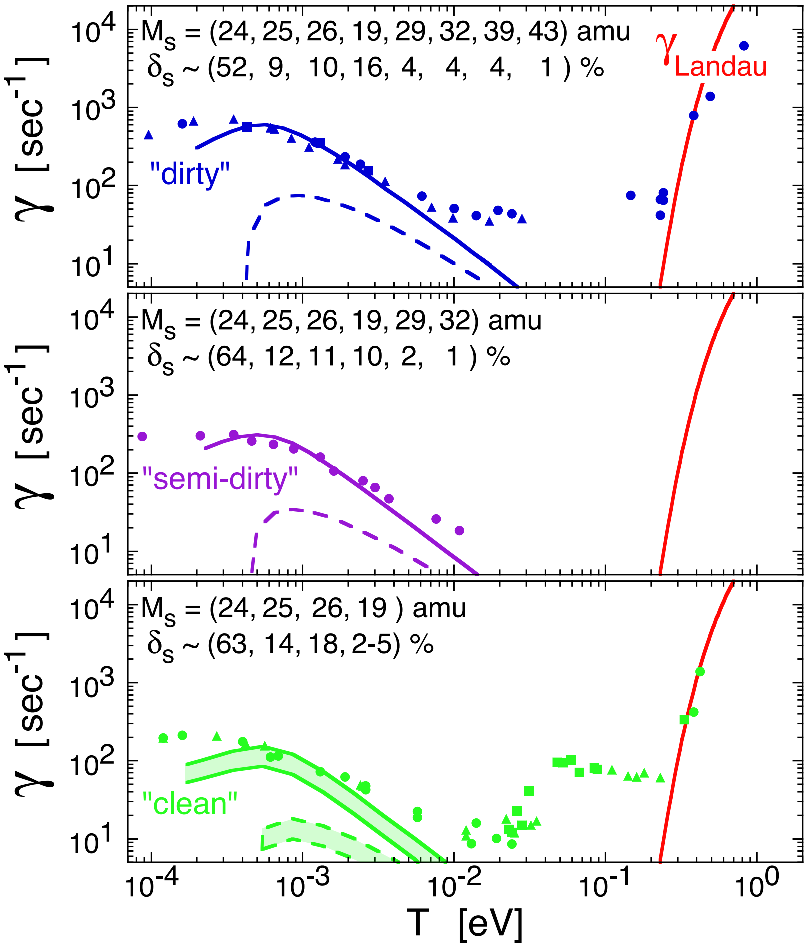

Figure 4.2: Symbols are damping measurements on plasmas with three different species compositions and a density $n_0 \sim 1.9 \times 10^7$ cm^{-3}. Curves for $T < 10^{-2}$ eV correspond to drag damping predictions for both a classical calculation that assumes only short-range collisions (dashed), and a calculation including the new long-range enhanced collisional slowing (solid).

4.5 Drag Damping Theory

This inter-species drag damping can be understood from cold fluid theory. Basically, ions are accelerated by the wave electric field as eE/M_s, producing a disparity in the velocity of different species. Inter-species collisions then cause drag forces on each species, which damps the wave. The wave particle velocity of species s parallel to the magnetic field is

$$\delta \mathrm{v}_s = \frac{e k_z \delta\phi}{M_s \omega} - i \sum_{s'} \frac{\nu_{ss'}}{\omega} \left(\delta \mathrm{v}_s - \delta \mathrm{v}_{s'} \right), \tag{4.2}$$

where $\nu_{ss'}$ is the collisional slowing rate between species s and s', $\delta\phi$ is the wave potential, and ω is the complex wave frequency.

We are able to directly measure the velocities of the three Mg^+ isotopes by measuring the parallel velocity distribution $F(\mathrm{v}_\|)$ coherent with the wave-phase $\theta_w(t)$ received on the wall. Figure 4.3 (Top) shows the wave-phase coherent $F(\mathrm{v}_\|)$ of the Mg^+ isotopes for 8 different phase bins $\theta_l = (l-1)2\pi$. The Mg^+ distributions oscillate around their respective $\mathrm{v} = 0$ (yellow lines) as the ions are accelerated by the wave electric field. Here a large amplitude drive of 20 $\mathrm{mV_{pp}}$ has been used to induce a fluid velocity $\mathrm{v}_f^{(24)} = 77$ m/s comparable to the thermal speed $\bar{\mathrm{v}}$.

The black symbols and curves in Figure 4.3 (Bottom) are measurements of and sine wave fits to the central velocity of each isotope distribution for the 8 different phase bins. These fits determine the fluid velocity of each Mg^+ isotope. The velocity difference $\delta \mathrm{v}_f^{(s)} \equiv \mathrm{v}_f^{(s)} - \mathrm{v}_f^{(24)}$ of the isotopes $^{25}\mathrm{Mg}^+$ and $^{26}\mathrm{Mg}^+$ are represented by the red curves. We find $\delta \mathrm{v}_f^{(25)} = -(4.1 \pm 1.1)\%\, \mathrm{v}_f^{(24)}$ and $\delta \mathrm{v}_f^{(26)} = -(8.2 \pm 1.1\%)\, \mathrm{v}_f^{(24)}$ in agreement with the relative 4% and 8% increases in the respective isotopic masses.

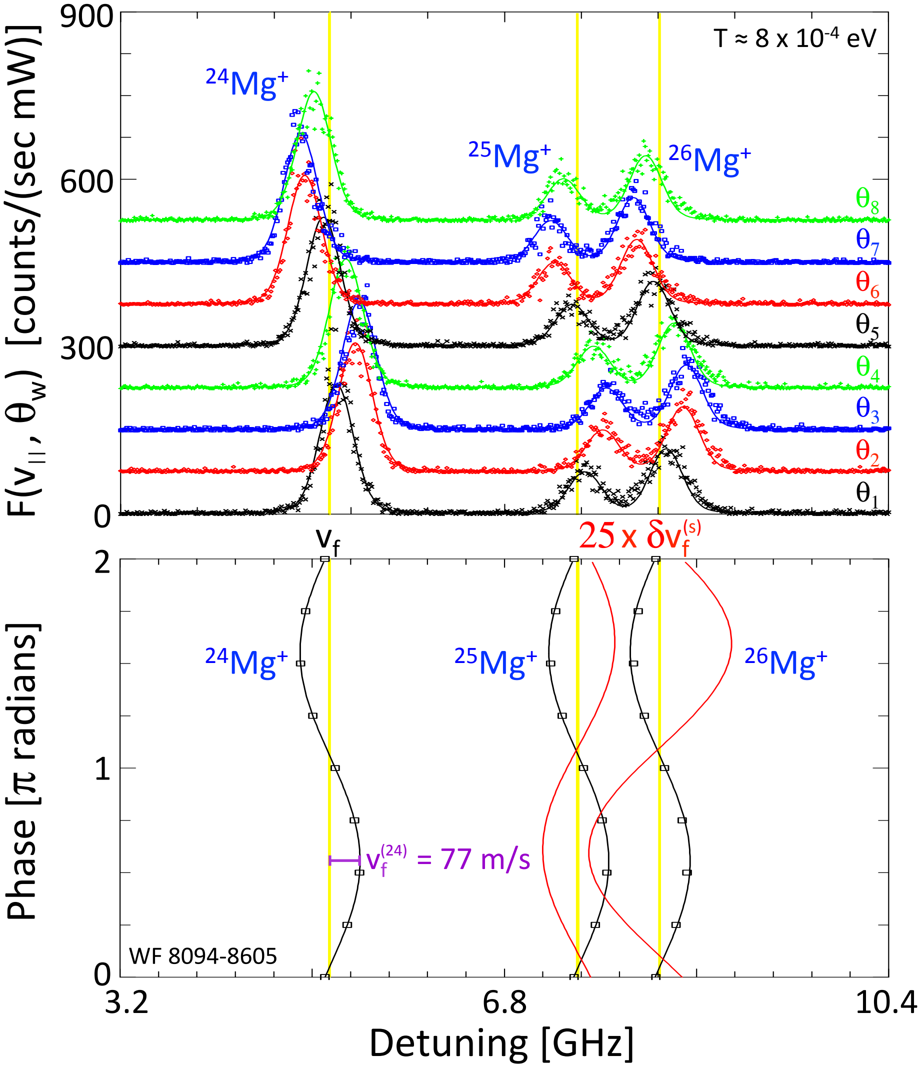

Figure 4.3: Measurements of the parallel velocity distribution function $F(\mathrm{v}_{\|})$ coherent with the wave-phase $\theta_w(t)$ (Top), each phase is offset for clarity. Black symbols and curves (Bottom) are measurements of and sine wave fits to the central velocity of the oscillating Mg$^+$ distributions. Red curves (Bottom) are 25× the relative velocity of the Mg$^+$ isotopes to that of ^{24}Mg$^+$.

For azimuthally symmetric waves, the drag damping is calculated by solving for the complex $\omega = \omega_r + i\gamma$ in the linearized Poisson equation,

$$\frac{1}{r}\frac{\partial}{\partial r}\left(r\frac{\partial\delta\phi}{\partial r}\right) - k_z^2\delta\phi = -\frac{4\pi e k_z}{\omega}\sum_s n_{0s}\delta \mathrm{v}_s \tag{4.3}$$

using the shooting method. Here, the linearized continuity equation $\delta n_s = k_z n_{0s}\delta\mathrm{v}_s/\omega$ has been used to replace the perturbed density δn_s with the species velocity $\delta\mathrm{v}_s$. Also, the equilibrium density n_{0s} has radial dependence at low temperatures when centrifugal mass separation becomes important. The collisional drag damping rate γ is proportional to the rate of collisional slowing $\nu_{ss'}$.

For plasmas that are both radially uniform and have weak collisionality ($\nu_{ss'} \ll \omega_{TG}$), the collisional drag damping can be solved analytically as

$$\gamma \equiv \mathrm{Im}(\omega) = \frac{1}{4\omega_p^2}\sum_s\sum_{s'}\frac{(M_{s'} - M_s)^2}{M_{s'}^2}\omega_{p,s}^2\nu_{ss'}, \tag{4.4}$$

where $\omega_{p,s}^2 = 4\pi e^2 n_s/M_s$ is the species plasma frequency, and $\omega_p^2 = \Sigma\omega_{p,s}^2$ is the total plasma frequency. This equation is valid in the regime $T \gtrsim 10^{-3}$ eV for the plasmas considered in these experiments. Equation 4.4 recovers the electron-ion drag damping results of Lenard and Bernstein [56] for neutral plasmas. Here, an enhancement of $\nu_{ss'}$ from long-range collisions will increase the drag damping.

4.6 Long-Range Collisionality

Recent theory [12] has shown that two types of long-range collisions occur, separated by the newly identified diffusion scale length $d \equiv b(\bar{\mathrm{v}}^2/b^2\nu_{ss'}^2)^{1/5} \propto T^{1/5}$, where $b = e^2/T$ is the distance of closest approach. The present experiments cover a range in temperature $10^{-4} \lesssim T \lesssim 1$ eV, corresponding to a range in the diffusion scale length $33 \lesssim d \lesssim 135$ μm. For impact parameters $\rho < d$, collisions occur faster than the diffusion timescale, so they can be regarded as isolated Boltzmann collisions. In contrast, for $\rho > d$, multiple weak collisions occur simultaneously and particles diffuse in velocity, so Fokker-Planck theory is required. The predicted slowing-down rate has the "classical" scaling with an enhanced Coulomb logarithm, specifically

$$\nu_{ss'} = \sqrt{\pi} n_{s'} \bar{\mathrm{v}}_{ss'} b^2 \ln \Lambda, \tag{4.5}$$

where

$$\bar{\mathrm{v}}_{ss'} \equiv \sqrt{2T\mu}/M_s, \tag{4.6}$$

$$\mu \equiv M_s M_{s'}/(M_s + M_{s'}) \tag{4.7}$$

is the reduced mass, and

$$\ln \Lambda = \frac{4}{3} \ln\left(\frac{\min[r_c, \lambda_D]}{b}\right) + p \ln\left(\frac{d}{\max[b, r_c]}\right) + 2 \ln\left(\frac{\lambda_D}{\max[d, r_c]}\right) \tag{4.8}$$

is the enhanced Coulomb logarithm. The first logarithmic term in Eq. 4.8 is from classical short-range, Boltzmann collisions. The collisional slowing rate is enhanced by the second and third terms, which represent long-range Boltzmann and Fokker-Planck collisions respectively. For repulsive (like-sign) collisions $p = 5.899$; whereas, $p = 0$ for attractive (opposite-sign) collisions in neutralized plasmas.

In Fig. 4.4, these short and long-range collision rates are plotted over a range in temperature for our typical "dirty" plasma. Long-range, 1D Boltzmann collisions

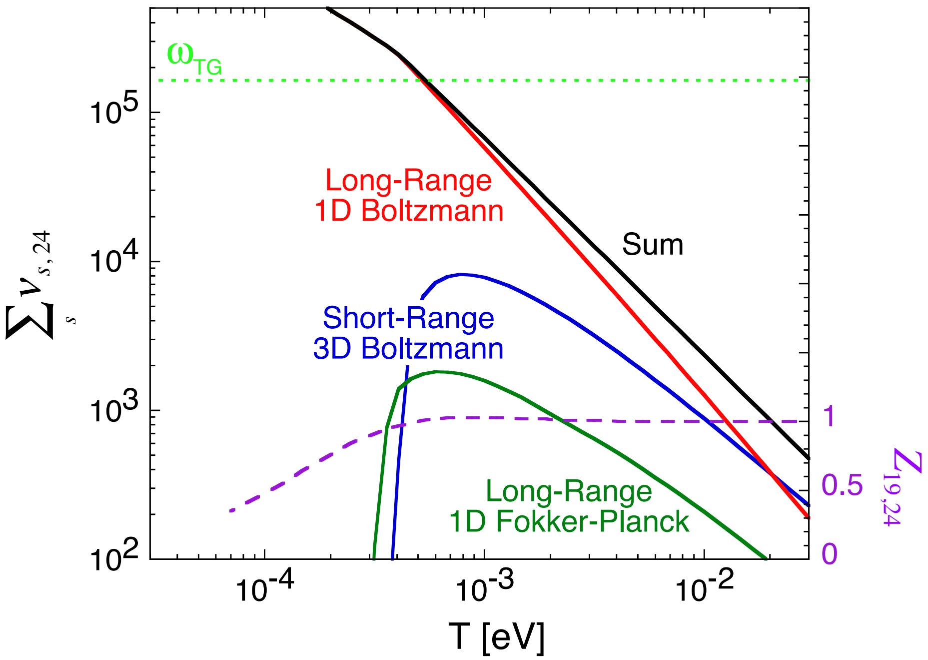

Figure 4.4: Short and long-range collision rate versus temperature for a typical “dirty” plasma. The dashed purple line is the radial overlap between species ^{24}Mg$^+$ and H_3O^+.

clearly dominate the collisionality in these plasmas, exceeding the classical short-range collision rate by as much as an order of magnitude. At low temperatures $T < 4 \times 10^{-4}$ eV, the plasma becomes strongly magnetized (i.e. $r_c < b$), and the short-range collision rate approaches zero, because the cyclotron energy of the colliding pairs is an adiabatic invariant [57]. Long-range, 1D Fokker-Planck collisions are rather weak, and approach zero for $T \lesssim 3 \times 10^{-4}$ eV when $\lambda_D < d$.

Predictions of the drag damping theory for both a classical calculation that assumes only short-range collisions (dashed), and a calculation including the new long-range enhanced collisional slowing (solid) are shown in Fig. 4.2. Theory is in quantitative agreement with the experimental results only when long-range collisions are included, exceeding predictions considering only short-range collisions by as much as an order of magnitude.

The discrepancy between theory and experiments around 10^{-2} eV may be a result of another damping mechanism. Cold fluid theory predicts that these TG waves are also damped from viscous momentum transfer along and across the magnetic field [58]. In this temperature regime, this damping is too weak ($\gamma \sim 5$ s^{-1}) to explain the discrepancy we observe, but an enhancement of this damping is predicted from finite-length effects [59]. Bounce harmonic Landau damping is another mechanism that may increase the damping in this temperature regime.

4.7 Centrifugal Separation and Fluid Locking

At $T \lesssim 10^{-3}$ eV, the measured and predicted drag damping rates decrease from the collisional $T^{-3/2}$ scaling. We analyze two effects that contribute to this decrease. First, the ions begin to centrifugally separate by mass, with the lighter ions near $r = 0$. In Fig. 4.4, the dashed purple curve represents the radial overlap between species $s = {}^{24}\mathrm{Mg}^+$ and $s' = \mathrm{H_3O^+}$, defined as

$$Z_{ss'} \equiv \frac{2\int_0^{R_p} \delta_s(r)\delta_{s'}(r) r dr}{\delta_s \delta_{s'} R_p^2}. \tag{4.9}$$

On warm plasmas $T \gtrsim 10^{-3}$ eV, the species are radially uniform and $Z_{ss'} = 1$. However, as the species centrifugally separate, $Z_{ss'}$ decreases, approaching zero for complete radial separation. This reduction in the radial species overlap decreases the inter-species drag. Of course, $Z_{ss'}$ represents radially local collisions only, and non-local interactions will persist even with complete radial separation.

Secondly, the collisionality approaches the wave frequency ω_{TG} around $T \sim 10^{-3}$ eV, as shown in Fig. 4.4. For $\nu \sim \omega_{TG}$, the species collide before developing a disparity

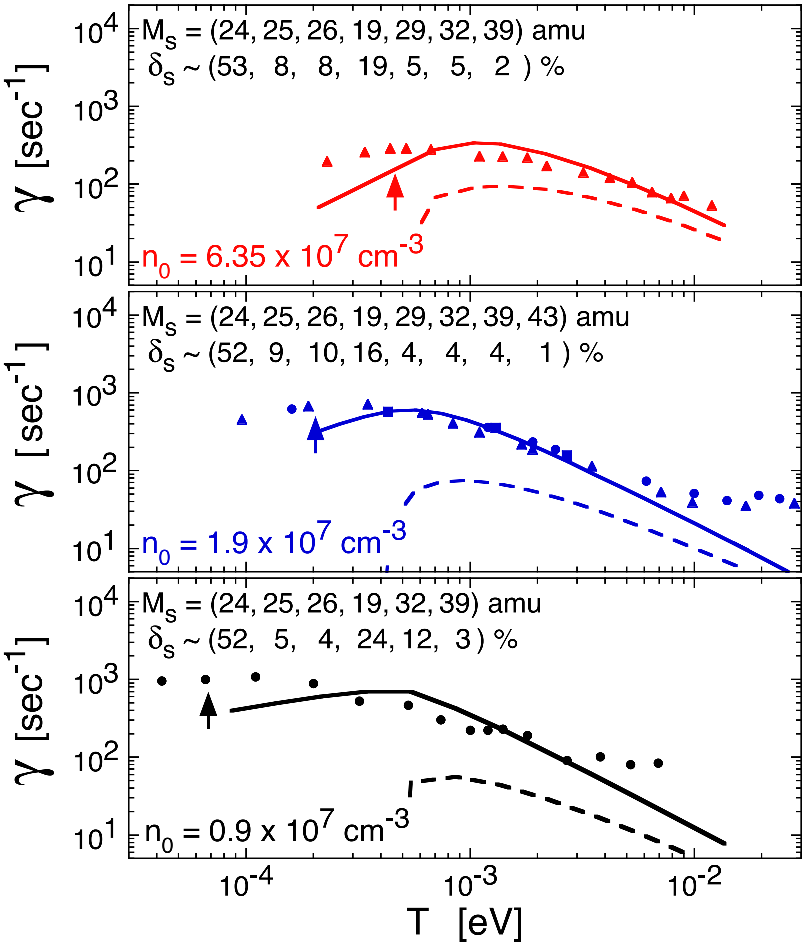

Figure 4.5: A narrower temperature range focusing on measurements of drag damping for three different density plasmas with different compositions. Symbols are measurements and curves are theory predictions assuming either classical collisions (dashed) or long-range enhanced collisions (solid). Arrows indicate the temperature of peak measured damping.

in velocity. In essence, the species fluid elements begin to collisionally lock, which decreases the drag.

Both fluid locking and centrifugal separation are dependent on the plasma density. Figure 4.5 focuses on the narrower temperature regime of drag damping for three different density plasmas. A similar quantitative agreement with long-range enhanced drag damping theory is observed as the density is changed by a factor of 7. However, as the density increases, centrifugal separation and fluid locking occur at higher temperatures, and a corresponding increase in the temperature of the measured "peak" damping is observed. These results suggest that fluid locking and centrifugal separation are at least in part responsible for the decrease in the damping from the $T^{-3/2}$ scaling.

To isolate how reducing the radial overlap between species influences the drag damping, we use the fact that the plasma thermally equilibrates on a faster timescale than the species diffuse radially. This enables, for a short period of time, the creation of a warm plasma with a reduced $Z_{ss'}$. Figure 4.6 depicts the details of this process. The plasma is initially cooled to a low temperature $T \sim 10^{-4}$ eV, where the species are centrifugally separated by mass. At $r = 0.3$ cm on a $R_p = 0.5$ cm plasma, Fig. 4.6a shows the measured $^{25}\text{Mg}^+$ and $^{26}\text{Mg}^+$ peaks (blue) as 2× and 4× smaller than expected for a uniform species distribution. A 500 mV$_{pp}$, 200 cycle burst at 36 kHz is applied to the plasma end at 20 ms, heating the plasma. In Fig. 4.6c, the plasma temperature is shown to re-equilibrate after this heating burst to $T \sim 3 \times 10^{-3}$ eV on a 20 ms timescale. But, on this timescale, the species have not remixed radially (Fig. 4.6b). The species generally remix in about 500 ms. By exciting a wave before the species have remixed (Fig. 4.6d), we are able to measure the drag damping on a warm plasma with a reduced radial species overlap. This process can be repeated for different heating burst amplitudes to change the plasma temperature and hence collisionality, while keeping the species overlap $Z_{ss'}$ roughly constant.

Figure 4.7 shows damping measurements on a standard "dirty" plasma for which the overlap integral $Z_{19,24}(T)$ results from centrifugal separation at the abscissa T; and on the same "dirty" plasma for which the radial species overlap is kept small and constant at $Z_{19,24} \sim 0.43$ determined by the initial $T \sim 10^{-4}$ eV. Clearly, reducing the

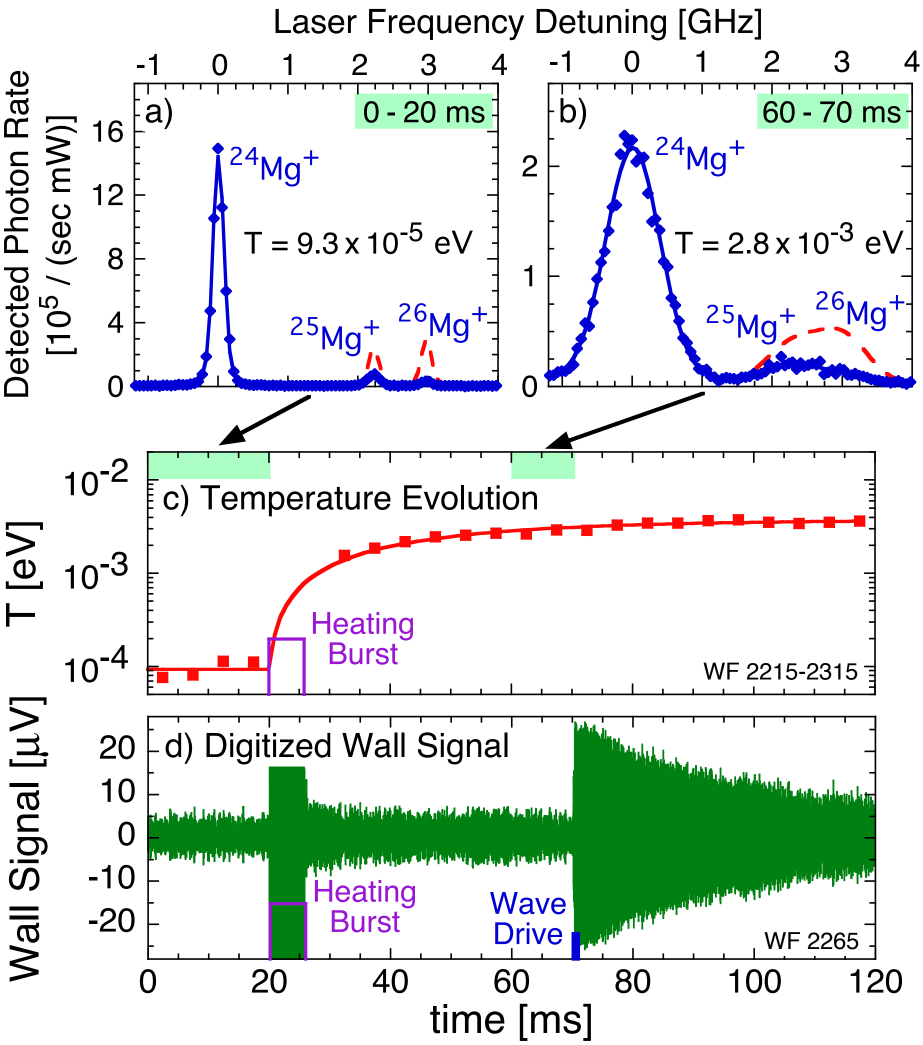

Figure 4.6: Process for creating a warm plasma with reduced radial overlap between the species. The blue curves of (a) and (b) are the measured Mg$^+$ distributions at a radius of 0.3 cm before and after a heating burst; and the red dashed curves are what the distributions would look like on a radially uniform plasma. The plasma temperature equilibrates (c) before the species have remixed, enabling damping measurements (d) on a warm but radially non-uniform plasma.

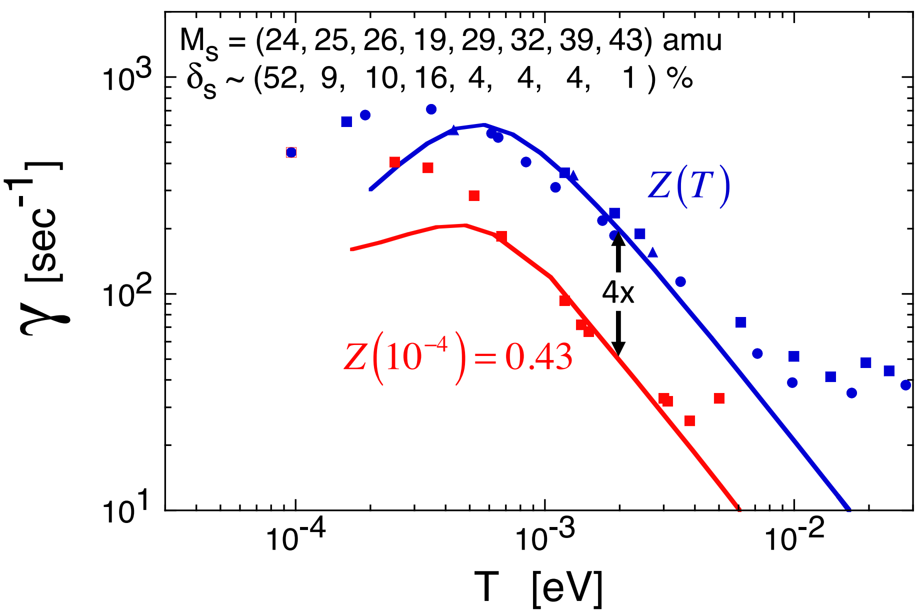

Figure 4.7: Measurements of drag damping on a typical "dirty" plasma with centrifugal separation determined by the abscissa T (blue); and on a plasma with the same "dirty" composition but with a reduced radial species overlap $Z_{19,24} \sim 0.43$ determined by the initial $T \sim 10^{-4}$ eV (red).

species overlap reduces the drag damping. At $T \sim 2 \times 10^{-3}$ eV, $Z_{19,24}$ differs from 1 to 0.43, and the damping rate is reduced by a factor of 4. The agreement between theory and experiments for $T \gtrsim 6 \times 10^{-4}$ eV demonstrates that the influence of centrifugal separation is properly modeled by radially local collisions in this temperature regime. The data for $T < 6 \times 10^{-4}$ eV is inconclusive.

The effect that collisional locking of the species fluid elements has on the drag damping is investigated by measuring the damping rate of higher frequency, axial modes. This inter-species drag damping depends on the disparity in the species velocity, and not on the axial mode structure, so higher frequency axial modes are predicted to have the same damping rate. However, collisional locking occurs when the collisionality approaches the wave frequency, so a higher frequency modes will have less fluid locking.

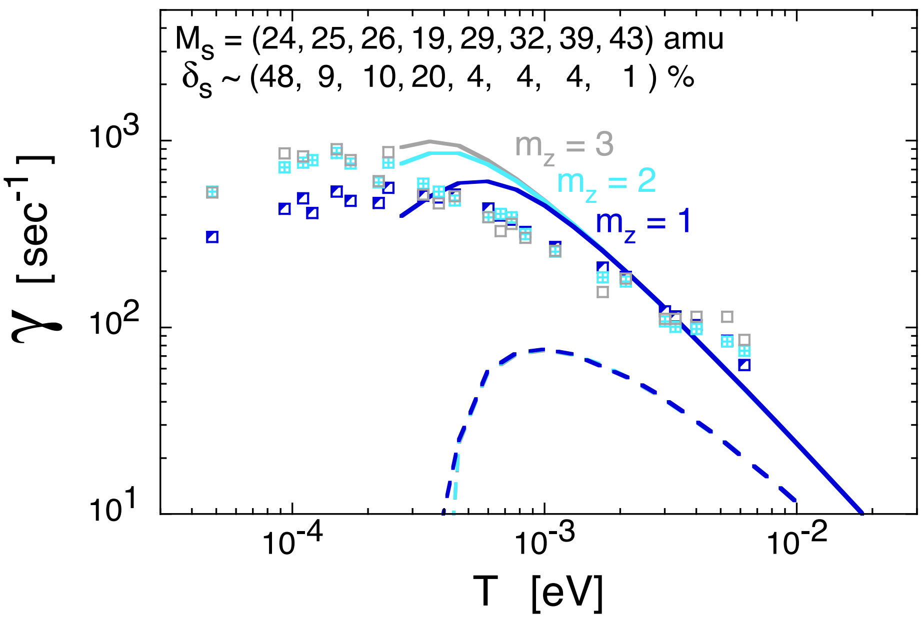

Figure 4.8: Drag damping measurements on higher frequency, axial modes with $f_1 = 27.25$ kHz, $f_2 = 50.35$ kHz and $f_3 = 68.45$ kHz. Dashed lines are theory curves assuming classical collisions and solid curves are that same theory assuming long-range enhanced collisions.

Figure 4.8 shows the damping rate of the first three axial modes ($m_z = 1$, 2, and 3). For $T \gtrsim 3 \times 10^{-4}$ eV, the higher frequency modes are all damped at the same rate, as predicted by theory in the weak collisionality regime. In contrast, below $T \lesssim 3 \times 10^{-4}$ eV, the higher frequency modes are more heavily damped, which suggests less fluid locking. This stronger damping is in qualitative agreement with theory, which predicts a factor of 2 increase in the damping rate for $m_z = 3$ at $T = 3 \times 10^{-4}$ eV.

In general, these TG waves are more heavily damped than the current theory prediction at ultra-low temperatures $T \lesssim 4 \times 10^{-4}$ eV. In this centrifugally separated temperature regime, non-local interaction may be significant, which are not included in the current theory. Also, for the typical density $n_0 = 1.9 \times 10^7$, the plasma ions becomes moderately correlated, with correlation parameter $\Gamma \equiv e^2/aT \gtrsim 0.2$ for $T \lesssim 4 \times 10^{-4}$ eV, where $a = (3/4\pi n_0)^{1/3}$ is the Wigner-Seitz radius. Correlations may limit the parallel collisionality [60, 61], decreasing the effects of fluid locking and increasing the predicted damping rates.

4.8 Conclusion

In summary, measurements of collisional inter-species drag damping have provided the first experimental confirmation of the long-range enhanced, parallel collisional slowing rate. We presented collisional drag damping theory, which is in quantitative agreement with the experimental results for a range of plasma compositions and densities only when long-range collisions are included. At low temperatures $T \lesssim 10^{-3}$ eV, the damping is observed to be reduced from the typical $T^{-3/2}$ collisional scaling as centrifugal separation and fluid locking become significant. Non-local interactions and correlations may be responsible for the discrepancies between theory and experiments at ultra-low temperatures.

4.9 Acknowledgements

This chapter, in part, is currently being prepared for submission for publication. M. Affolter, F. Anderegg, D.H.E. Dubin and C.F. Driscoll. The dissertation author was the primary experimentalist and author of this material. Dubin previously developed and published the long-range collision theory as Ref. [12].

Chapter 5

Non-Linear Langmuir Waves

5.1 Introduction

This chapter describes experiments and theory on the fundamentals of non-linear wave couplings, using pure ion plasmas as the model system. This is partially motivated by non-linear phenomena observed when high power lasers impinge on plasmas. In these laser-plasma interactions, the high intensity laser couples to ion acoustic waves (IAWs), causing scattering of the electromagnetic waves. This process, called stimulated Brillouin scattering (SBS), is a concern for inertial confinement fusion, as it may reduce the laser energy coupled into the fusion capsule, or reduce the spherical symmetry. Experiments have shown that SBS saturates at high laser intensities [62, 63, 64, 65]. Several non-linear effects have been postulated to explain this saturation, including non-linear frequency shifts [66, 67], and the parametric decay of the driven IAW into two daughter waves [68, 69, 70, 71, 72]. The near-acoustic dispersion relation of cold IAWs is similar to the dispersion of Langmuir waves on our confined ion plasmas, so the fundamental non-linear effects should be similar.

Here we experimentally quantify non-linear effects in Langmuir waves, including harmonic generation, non-linear frequency shifts, and the parametric decay instability. These experiments are conducted on well-controlled, laser-diagnosed, pure ion plasmas confined in a Penning-Malmberg trap. The plasma waves are azimuthally symmetric standing waves, discretized by the axial wavenumber $k_z = m_z(\pi/L_p)$. The dispersion $\omega(k)$ is basically acoustic, i.e. $\omega(k) \propto \mathrm{v}_{ph}k(1-\epsilon k^2)$ with $\epsilon \propto R_p/L_p$. By varying the plasma length, experiments are conducted on plasmas with different deviations from acoustic dispersion.

At large wave amplitudes, the detected wave density perturbation is no longer a simple sinusoid. We observe frequency harmonics corresponding to a steepening of the wave density perturbation, and non-linear frequency shifts of the fundamental. Both the harmonic content and the relative frequency shifts are more prominent when the dispersion is more nearly acoustic.

The wave-wave coupling rates are measured between large amplitude $m_z = 2$ waves and small amplitude $m_z = 1$ waves, which have a small frequency detuning $\Delta\omega = 2\omega_1 - \omega_2$. The *large* wave amplitude is characterized by the parametric coupling strength $\Gamma_0 \equiv (\delta n_2/n_0)(\omega_1+\omega_2)(R/8)$, where $R \sim 0.85$ is the radial coupling coefficient. We find that the relative amplitudes of Γ_0 and $\Delta\omega$ are fundamental to the overall wave-wave interaction. At small excitation amplitudes ($2\Gamma_0 < \Delta\omega$), this detuning causes the $m_z = 1$ mode amplitude to “bounce” at rate $\omega_B \approx \Delta\omega$ with amplitude excursions $\Delta A_1 \propto (\delta n_2/n_0)$, in quantitative agreement with three-wave theory [13]. At larger excitation amplitudes ($2\Gamma_0 > \Delta\omega$), phase-locked exponential growth of the $m_z = 1$ mode is observed, consistent with the three-wave instability analysis [13]. Near the decay threshold $2\Gamma_0 \sim \Delta\omega$, an unexpected slow average growth of the bouncing

$m_z = 1$ wave amplitude is observed, which may be a result of the plasma evolving during the wave-wave interaction.

5.2 Details of the TG Dispersion Relation

As discussed in Sec. 4.3, the linear dispersion relation of Langmuir waves in trapped plasmas is near-acoustic, because of the shielding of the confinement electrodes at R_w. In this section, we investigate the details of this deviation from acoustic dispersion. The Trivelpiece-Gould (TG) dispersion relation [52, 53] for cold, azimuthally symmetric, z-periodic travelling waves on a "top-hat" plasma of radius R_p is approximately

$$\omega_{m_z} = \omega_p \frac{k_z/k_\perp}{\sqrt{1+(k_z/k_\perp)^2}}, \tag{5.1}$$

where $k_z \equiv m_z(\pi/L_p)$ and $k_\perp = R_p^{-1}[2/\ln(R_w/R_p)]^{1/2}$ are the axial and transverse wavenumbers respectively, and $\omega_p = \sqrt{4\pi e^2 n_0/M_s}$ is the plasma frequency. However, in comparison to experiments, neither k_z nor $k_\perp$ are definable to better than 10%. For our trapped plasmas of length L_p, two counter propagating $\pm k_z$ traveling waves with phase velocity $\mathrm{v}_{ph} = \omega/k_z$ create a standing wave perturbation. These standing wave resonances occur when the traveling wave and its reflections from the plasma ends are in phase.

These waves are excited from a confinement ring located near the plasma end, and the resulting wave is detected as induced image charge on an off-center ring, as shown in the Fig. 5.1 inset. Typically, a 40 cycle sine wave burst with an amplitude $A_B \sim 50 - 100$ mV$_{pp}$ is used. These bursts are ramped to/from full amplitude over 4 cycles to prevent excitation of other waves. By the end of the burst, the plasma has been heated from $T \sim 2 \times 10^{-3}$ eV to $T \gtrsim 10^{-2}$ eV. At this temperature, few particles are resonant with the wave $\mathrm{v}_{ph}/\bar{\mathrm{v}} \sim 28$ and Landau damping is negligible; here the waves damp through collisions at a rate $\gamma \sim 100$ /s, as discussed in Sec. 4.4.

Figure 5.1 shows frequency measurements of several small amplitude ($A_B \sim 2$ mV$_{pp}$) TG modes for two different plasma lengths. We see that the measured mode frequencies (symbols) are nearly acoustic (dashed lines), and that the deviation from acoustic dispersion is dependent on the plasma geometry ($k_\perp/k_1$). When the plasma length is increased from 13.6 cm to 20.3 cm (blue to red data), the relative deviation from acoustic dispersion $\Delta\omega/\omega_1$ is reduced by about 50%. The on-axis plasma length is varied over the range $12.4 \lesssim L_p \lesssim 20.3$ cm by varying the strength of the confining potentials, enabling a corresponding control of the mode frequencies $23.8 \gtrsim \omega_1/2\pi \gtrsim 13.7$ kHz and detuning $3.1 \gtrsim \Delta\omega/2\pi \gtrsim 0.85$ kHz.

The curves in Fig. 5.1 are predictions of Eq. 5.1 with different transverse wavenumbers. Theory defines $k_\perp = R_p^{-1}[2/\ln(R_w/R_p)]^{1/2}$. This approximation is valid for plasmas with $m_z\pi R_w/L_p \ll 1$ and $R_p/R_w \ll 1$. We find that for the plasmas in these experiments with $\pi R_w/L_p \sim 0.6$ and $R_p/R_w \sim 0.2$ that the measured $m_z = 1$ mode frequency is in agreement with this approximate $k_\perp$ prediction if L_p is increased by approximately 10% (dotted curves). However, this approximate $k_\perp$ prediction fails to explain the large deviation from acoustic dispersion of the higher axial modes for reasonable 10% variations in the plasma parameters (L_p, R_p, and n_0).

The discrepancy in the frequency for the higher k_z modes is result of $k_\perp$ having a slight k_z dependence for these short plasmas, which is ignored in the typical approximation. The transverse wavenumber $k_\perp$ is determined by the boundary condition that the radial wave potential be continuous at the plasma radius [52, 53]

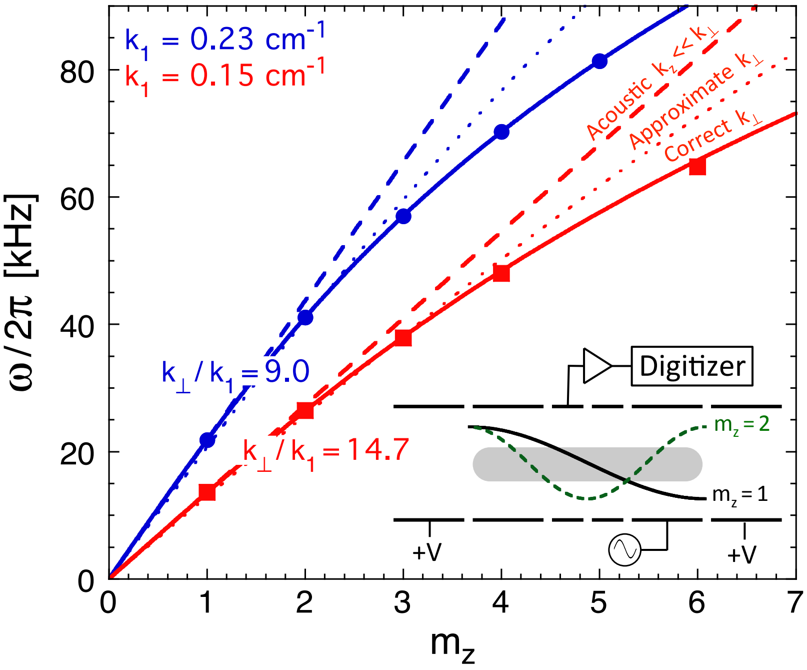

Figure 5.1: Measured TG dispersion relation (symbols) for two different plasma geometries compared against cold fluid theory. Dashed lines are acoustic dispersion relations, and dotted/solid curves are TG dispersion relations with approximate/correct $k_\perp$. The experimentally measured density n_0 and plasma radius R_p are used for the theory predictions with a slightly increased plasma length of approximately $1.1L_p$. The inset is a sketch of the typical confinement geometry and the two lowest order modes.

given by

$$k_\perp R_p \frac{J_0'(k_\perp R_p)}{J_0(k_\perp R_p)} = k_z R_p \frac{I_0'(k_z R_p) K_0(k_z R_w) - I_0(k_z R_w) K_0'(k_z R_p)}{I_0(k_z R_p) K_0(k_z R_w) - I_0(k_z R_w) K_0(k_z R_p)} \tag{5.2}$$

for $m_\theta = 0$ modes in a strong magnetic field. For a plasma with $L_p = 13.6$ cm and $R_p = 0.48$ cm, Eq. 5.2 determines $k_\perp \approx 1.96 + 0.12 m_z$. This slight increase of $k_\perp$ for the higher axial modes increases the deviation from acoustic dispersion in agreement with the experimental results (solid curves).

5.3 Harmonic Generation

At large wave amplitudes, harmonic generation steepens and increases the peak wave density perturbation. The detected voltage on the wall of a large amplitude m_z standing mode has the functional form

$$V(t) \propto \sum_j A_{m_z}^{(j)} \cos(j k_z z) \cos(j \omega_{m_z}), \tag{5.3}$$

where $j = 1, 2, 3, \ldots$ correspond to phase-locked frequency harmonics of the fundamental, and $A_{m_z}^{(j)} = \delta n_{m_z}^{(j)} / n_0$ is the amplitude of these harmonics. Experimentally, we measure $V(t)$ with harmonic content at $j\omega_{m_z}$. Gauss's law relates the detected wall voltage $V_{m_z}^{(j)}$ of the $\cos(j k_z z)$ term to the wave density perturbation $\delta n_{m_z}^{(j)} / n_0$ as

$$\frac{\delta n_{m_z}^{(j)}}{n_0} = \left(\frac{j m_z \pi}{\hat{f}_{m_z}^{(j)} J_0(R_p k_\perp)} \right) \left(\frac{C}{q N_{tot}} \right) V_{m_z}^{(j)}, \tag{5.4}$$

where C is the capacitance of the electrode, $\hat{f}_{m_z}^{(j)} \equiv [\sin(j k_z (z_0 + L_D)) - \sin(j k_z z_0)]$, and z_0 is the axial location of the detection electrode of length L_D [11]. The accuracy

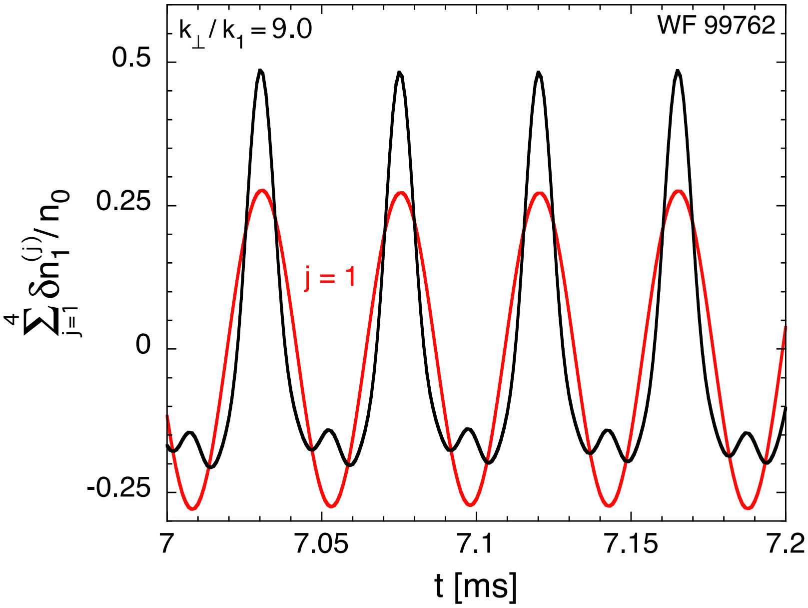

Figure 5.2: Detected waveform of a large amplitude $m_z = 1$ TG mode. The amplitude of the fundamental in shown in red, and the black curve includes the observe $j = 2$, 3, and 4 frequency harmonics.

of Eq. 5.4 is dependent on properly determining the plasma $n(r, z)$ equilibrium relative to the cylindrical detection electrodes, and is typically accurate to within 10% for the two lowest order modes. Note that to simplify the notation the superscript $j = 1$ is typically removed when referring to the fundamental density perturbation.

In Fig. 5.2, the detected temporal waveform of a large amplitude $m_z = 1$ mode is shown for a typical plasma with $k_\perp/k_1 = 9.0$. The wave density perturbation (black curve) includes frequency harmonics $j = 2$, 3, and 4. These harmonics lead to a peak density perturbation about twice the size of the fundamental (red curve). For this work, we describe the size of these non-linear waves by the amplitude of the fundamental density perturbation $\delta n_{m_z}/n_0$.

The amplitude of these frequency harmonics ($j = 2$, 3, and 4) is dependent on the size of the fundamental density perturbation, and on the deviation from acoustic dispersion. Figure 5.3 shows that the amplitude of the frequency harmonics

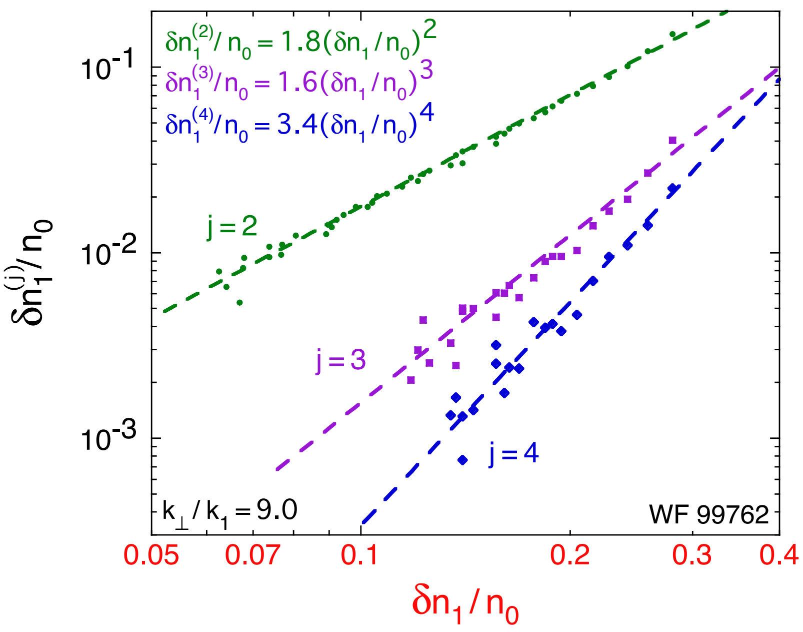

Figure 5.3: Measured amplitude of the frequency harmonics $j = 2$, 3, and 4 of a large amplitude $m_z = 1$ mode. Symbols are the amplitude measurements and curves are fits to the data.

is proportional to the fundamental density perturbation to the j^{th} power. We also observe larger harmonic content for more acoustic dispersion relations. When $\Delta\omega/\omega_1$ is reduced by 50% by making the plasma longer, we find roughly a factor of 2 increase in the $j = 2$ harmonic $A_1^{(2)}$.

5.4 Non-Linear Frequency Shifts

Along with this harmonic content, we observe a non-linear frequency shift of the fundamental. The symbols of Fig. 5.4 are measurements of the non-linear frequency shift of the $m_z = 1$ mode versus the wave density perturbation squared $(\delta n_1/n_0)^2$ for two different plasma geometries. These frequency shifts are proportional to $(\delta n_1/n_0)^2$, and increase as the plasma dispersion becomes more acoustic (increased $k_\perp/k_z$). To insure that these frequency shifts are measured at roughly the same temperature, the

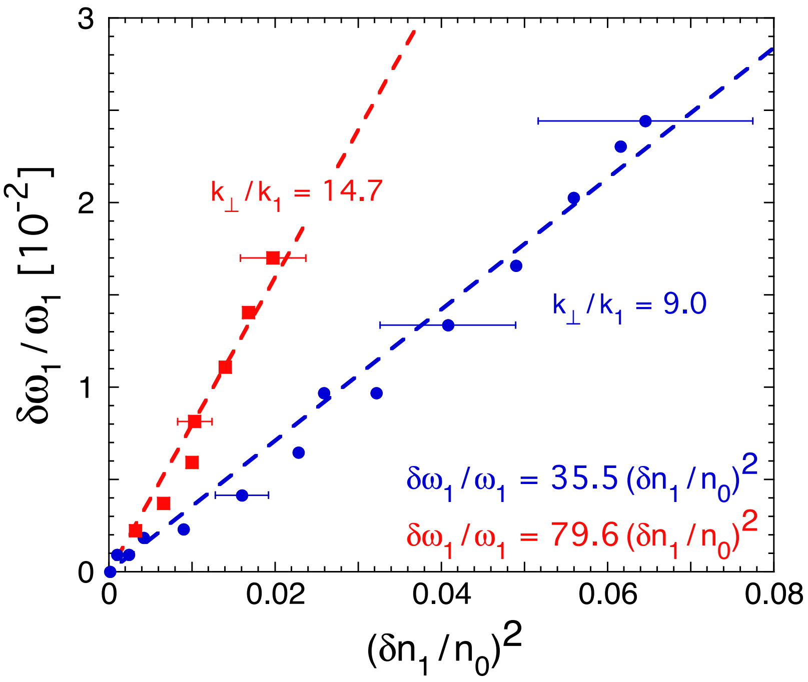

Figure 5.4: Symbols represent the measured percentage change of the $m_z = 1$ mode frequency versus the density perturbation squared for two different plasma geometries, and dashed lines are fits to the data.

measurements are made shortly after the drive as been turned off before wave damping heats the plasma. Similar density dependent frequency shifts have been observed in large amplitude IAW simulations [67, 66].

The observed harmonic content and non-linear frequency shifts are in qualitative agreement with a cold fluid theory that keeps higher harmonics of the fundamental [14]. This theory predicts similar amplitude scalings of the frequency harmonics, and an increase in both the harmonic content and the relative frequency shifts as the dispersion relation becomes more acoustic. However, the predicted magnitude of these effects are significantly larger than the observations. Presumably, finite-length effects are important in these experiments, which this periodic theory ignores.

5.5 Three-Wave Decay

Large amplitude $m_z = 2$ pump waves are predicted to parametrically couple to two $m_z = 1$ daughter waves enabling a decay instability. Experiments [71, 72] and simulations [68, 70] studying IAWs have observed this decay instability, but no quantitative experiments have been conducted. Cold fluid, three-wave theory predicts a threshold for the decay related to the deviation from acoustic dispersion by

$$\Gamma = \sqrt{\Gamma_0^2 - \left(\frac{\Delta\omega}{2}\right)^2} > 0, \tag{5.5}$$

where

$$\Gamma_0 = \frac{R}{4}\left(\frac{\omega_1 + \omega_2}{2}\right)\frac{\delta n_2}{n_0} \tag{5.6}$$

is the wave-wave coupling strength between the $m_z = 1$ and $m_z = 2$ modes, and $\Delta\omega = 2\omega_1 - \omega_2$ is the linear frequency detuning. When $2\Gamma_0 > \Delta\omega$, Γ is real and represents the exponential growth rate Γ_E of the $m_z = 1$ mode.

However, when $2\Gamma_0 < \Delta\omega$ the coupling strength cannot overcome the detuning. In this regime, the pump and daughter waves exchange energy in-and-out of phase resulting in the $m_z = 1$ mode amplitude to "bounce" at a rate $\omega_B = 2\bar{\omega}_1 - \omega_2$, where $\bar{\omega}_1$ is the frequency of the small amplitude daughter wave in the presence of the pump wave. Three-wave theory considering an infinitesimal daughter wave amplitude predicts frequency pulling

$$\delta\bar{\omega}_1 \equiv \bar{\omega}_1 - \omega_1 = \mathrm{Im}(\Gamma) - \Delta\omega/2 \tag{5.7}$$

towards resonance with the pump wave at $\omega_2/2$.

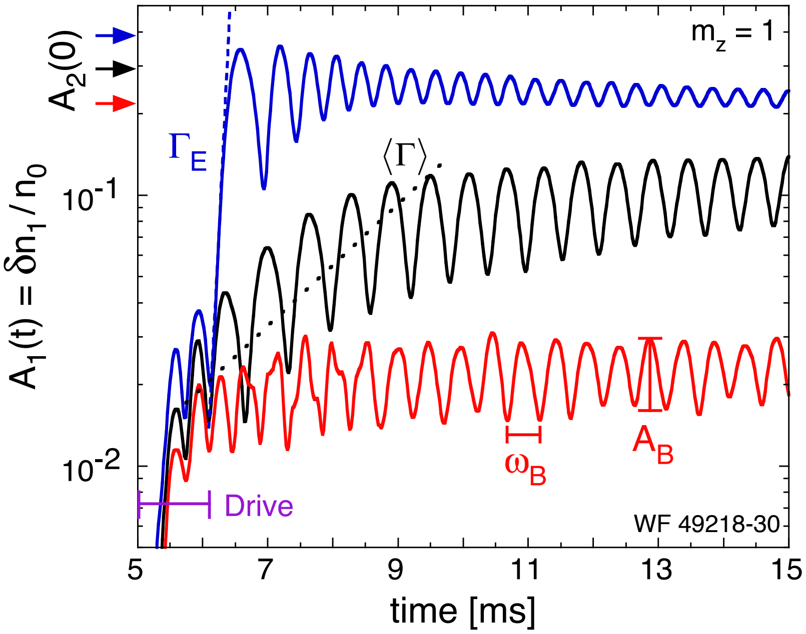

Figure 5.5: Amplitude evolution of the $m_z = 1$ mode for three different $m_z = 2$ amplitudes. Arrows indicate the initial pump wave amplitude, and here a 5% daughter wave seed is used.

5.6 Oscillatory Coupling and Exponential Growth Rates

Three different types of $m_z = 1$ amplitude evolutions are experimentally observed in the presence of different initial pump wave amplitudes, as shown in Fig. 5.5. Here a 5% $m_z = 1$ seed burst excites the daughter wave above the noise floor $(\delta n_1/n_0)_{\text{noise}} \sim 0.2\%$, and the wave amplitude is obtained by fitting the digitized wall signal in time segments of approximately 5 wave cycles with sine waves. Typically, to obtain the best fits, we digitally bandpass filter the recorded wave signal so that the pump and daughter wave amplitudes can be individually fit.

For small pump wave excitations (red curve in Fig. 5.5), the daughter wave amplitude "bounces" at a rate $\omega_B \approx \Delta\omega$ with amplitude excursions $A_B \propto A_1 A_2$

around an average $\langle A_1 \rangle$. At larger pump wave amplitudes (black curve in Fig. 5.5), the bounce frequency ω_B decreases and the amplitude excursions A_B increase. The amplitude modulation of the daughter wave can be modeled as

$$A_1(t) = \langle A_1 \rangle + A_B \sin(\omega_B t). \tag{5.8}$$

Using this model, we find that the rate of energy exchange between the pump and daughter waves is

$$\Gamma_{OCR} \equiv \frac{\dot{A}_1(0)}{A_1(0)} = \frac{A_B}{\langle A_1 \rangle} \omega_B; \tag{5.9}$$

identified here as the oscillatory coupling rate (OCR). This OCR provides a measure of Γ before the exponential growth regime. Figure 5.6 plots this Γ_{OCR} normalized to $\Delta\omega$ versus the normalized coupling strength for various detunings. We find that Γ_{OCR} is in quantitative agreement with three-wave theory independent of the deviation from acoustic dispersion.

As the pump wave amplitude nears the decay threshold ($2\Gamma_0/\Delta\omega \sim 1$), a slow average growth of the "bouncing" $m_z = 1$ wave amplitude is detected, as shown in Fig. 5.5. This average growth occurs at a rate $\langle \Gamma \rangle \lesssim 500$ s^{-1} $\sim 0.03\Delta\omega$ until $\delta n_1/n_0 \gtrsim 2\delta n_2/n_0$. At the moment, the cause of this average growth is unknown. This behavior may be a result of the plasma evolving during this wave-wave interaction, which is not considered in the three-wave analysis. Over the course of this "bouncing" average growth, the plasma heats as collisions damp the wave. A typical 10% density perturbation, once damped, results in an $\Delta T \sim 5 \times 10^{-3}$ eV increase in the plasma temperature. Also not considered by three-wave theory is the evolution in the wave frequencies. We showed in Sec. 5.3 that at these large amplitudes the wave frequencies are shifted away from their linear frequencies, so as the pump and daughter waves evolve in amplitude ω_B changes. At amplitudes near the decay threshold, $\omega_B \sim 0.5\Delta\omega$ and evolves to $\Delta\omega$ as the waves damp. Recent cold fluid theory that includes frequency harmonics [14] predicts a similar "bouncing" growth behavior, and connections with this theory are being pursued.

The dip in the three-wave theory coupling rate at $2\Gamma_0/\Delta\omega = 1$ corresponds to the daughter wave frequency being pulled by $\delta\bar{\omega}_1 = 0.5\Delta\omega$ into resonance with the pump wave. This implies that the rate of energy exchange $\omega_B \rightarrow 0$. Experimentally, we measure a reduction in the daughter wave frequency $\delta\bar{\omega}_1 \lesssim 0.2\Delta\omega$, and no dip in Γ_{OCR}. A possible cause for this discrepancy is that three-wave theory treats an infinitesimal daughter wave; whereas, experimentally to measure the $m_z = 1$ frequency and Γ_{OCR} the wave must be excited above the noise floor to $\delta n_1/n_0 \gtrsim 1\%$.

Exponential growth of the daughter wave is observed for $2\Gamma_0/\Delta\omega \gtrsim 1$ roughly consistent with three-wave theory. Here no $m_z = 1$ seed is used. The daughter wave grows above the noise floor, and the rate of this exponential growth is measured by fitting an exponentially growing sine wave to the digitized wall signal. In general, the rates $\Gamma_E \sim 3000 - 8000$ /s are obtained from fits over $5 - 10$ cycles of the growing $m_z = 1$ wave, and during this growth the $m_z = 2$ amplitude is about 20 times the $m_z = 1$ amplitude. As shown in Fig. 5.6, this rate of exponential growth scales roughly as the three-wave theory prediction, but is about 30% lower in magnitude.

It is surprising that three-wave theory is in such good agreement with the experimental results. This theory ignores the harmonic content and non-linear frequency shifts of the pump wave, which near the decay threshold are observed to increase the peak density perturbation by about 20% and decrease the detuning to $0.7\Delta\omega$.

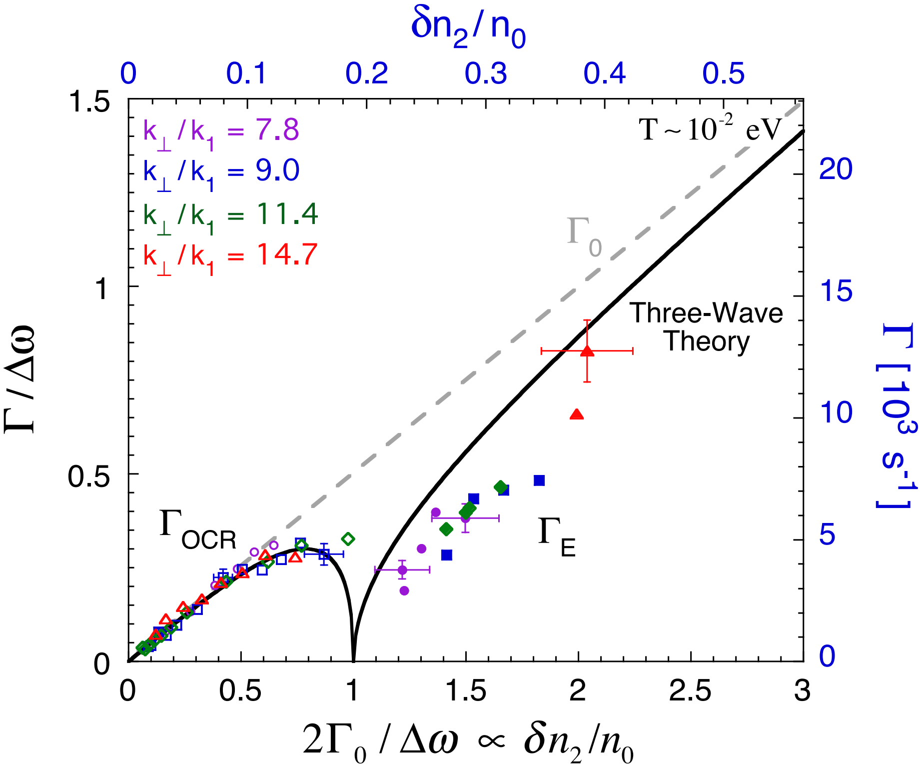

Figure 5.6: Measurements of the oscillatory coupling (open symbols) and exponential growth (closed symbols) rates normalized to $\Delta\omega$ versus the normalized coupling strength for various detunings. Solid black curve is three-wave theory, and the dashed grey line is the wave-wave coupling strength Γ_0.

Naively, one would expect that this reduction in the detuning would reduce the decay threshold to $2\Gamma_0/\Delta\omega \sim 0.7$. In further contradiction, recent cold fluid theory [14] with strong harmonic content and large non-linear frequency shifts predicts a stabilization of the decay instability, with decay thresholds $2\Gamma_0/\Delta\omega \gtrsim 4$. That is, the threshold of this decay is not yet understood.

Figure 5.7 shows RZ-Vlasov simulations for the experimental parameters of the typical $k_\perp/k_1 = 9.0$ plasma. At a temperature $T = 0.1$ eV, where Landau damping is negligible, these simulations show oscillatory coupling and exponential growth rates in agreement with the experimental results. Higher temperature simulations show a reduction in the instability threshold as kinetic effects become important. For the highest temperature of $T = 0.5$ eV, the ratio $\mathrm{v}_{ph}/\bar{\mathrm{v}} = 3$ indicates that Landau damping is strong. Previous experiments investigating the decay instability of higher axial modes ($\mathrm{m}_z = 4$ and 6) on hot electron plasmas [73] observed a decrease in the decay threshold as the plasma temperature was increased in qualitative agreement with these Vlasov simulations.

5.7 Conclusion

In summary, large amplitude Langmuir waves with a near-acoustic dispersion relation are shown to exhibit harmonic generation, non-linear frequency shifts, and a parametric decay instability. This harmonic content steepens the waveform, and can increase the peak wave density perturbation by as much as a factor of 2. These large amplitude waves have non-linear frequency shifts proportional to the wave density perturbation squared, and dependent on the relative deviation from acoustic dispersion. Surprisingly, three-wave theory that ignores these effects predicts oscillatory coupling

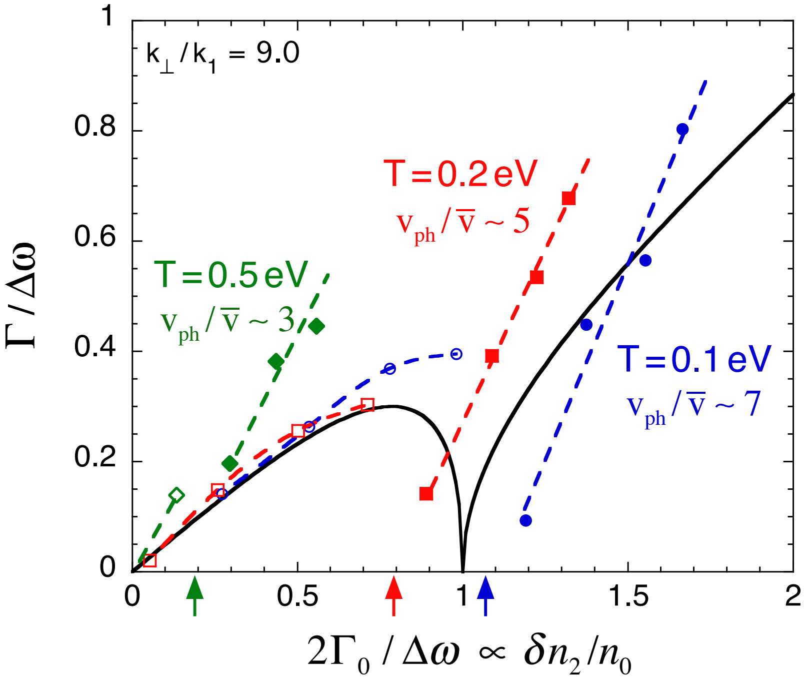

Figure 5.7: RZ Vlasov simulations of the decay instability for three different plasma temperatures. Open symbols are oscillatory coupling rates and closed symbols are exponential growth rates. Arrows indicate the instability threshold.

and exponential growth rates in agreement with the experimental results. However, near the decay threshold an unexpected average “bouncing” growth of the daughter wave is observed, which is presumably a result of the plasma evolving during the wave-wave interaction.

5.8 Acknowledgements

This chapter, in part, is currently being prepared for submission for publication. M. Affolter, F. Anderegg, D.H.E. Dubin, F. Valentini and C.F. Driscoll. The dissertation author was the primary investigator and author of this material.

Bibliography

[1] D. H. E. Dubin and T. M. ONeil, Reviews of Modern Physics **71**, 87 (1999).

[2] J. W. Britton, B. C. Sawyer, A. C. Keith, C.-C. J. Wang, J. K. Freericks, H. Uys, M. J. Biercuk, and J. J. Bollinger, Nature **484**, 489 (2012).

[3] R. S. Van Dyck Jr, D. Farnham, and P. Schwinberg, Phys. Rev. Lett. **70**, 2888 (1993).

[4] R. C. Davidson, *Physics of Nonneutral Plasmas*, volume 5, Addison-Wesley New York, 1990.

[5] F. Anderegg, X.-P. Huang, E. Sarid, and C. F. Driscoll, Review of Scientific Instruments **68**, 2367 (1997).

[6] A. G. Marshall, C. L. Hendrickson, and G. S. Jackson, Mass Spectrometry Reviews **17**, 1 (1998).

[7] E. Sarid, F. Anderegg, and C. F. Driscoll, Physics of Plasmas **2**, 2895 (1995).

[8] B. Roth, P. Blythe, H. Wenz, H. Daerr, and S. Schiller, Physical Review A **73**, 042712 (2006).

[9] B. C. Sawyer, J. G. Bohnet, J. W. Britton, and J. J. Bollinger, Physical Review A **91**, 011401 (2015).

[10] L.-K. Zhang, D. Rempel, B. N. Pramanik, and M. L. Gross, Mass Spectrometry Reviews **24**, 286 (2005).

[11] J. R. Danielson, F. Anderegg, and C. F. Driscoll, Phys. Rev. Lett. **92**, 245003 (2004).

[12] D. H. E. Dubin, Physics of Plasmas **21**, 052108 (2014).

[13] A. Ashourvan, Doctoral Dissertation, UCSD (2014).

[14] D. H. E. Dubin and A. Ashourvan, Physics of Plasmas **22**, 102102 (2015).

[15] R. A. MacGill, I. G. Brown, and J. E. Galvin, Review of Scientific Instruments **61**, 580 (1990).

[16] F. Anderegg, E. M. Hollmann, and C. F. Driscoll, Phys. Rev. Lett. **81**, 4875 (1998).

[17] T. M. O'Neil, Physics of Fluids **24**, 1447 (1981).

[18] D. Larson, J. Bergquist, J. Bollinger, W. M. Itano, and D. Wineland, Phys. Rev. Lett. **57**, 70 (1986).

[19] G. Andresen et al., Phys. Rev. Lett. **106**, 145001 (2011).

[20] D. H. E. Dubin, **1521**, 26 (2013).

[21] J. Adam, Plasma Physics and Controlled Fusion **29**, 443 (1987).

[22] R. Gilgenbach, M. Read, K. Hackett, R. Lucey, B. Hui, V. Granatstein, K. Chu, A. England, C. Loring, O. Eldridge, H. Howe, A. Kulchar, E. Lazarus, M. Murakami, and J. Wilgen, Phys. Rev. Lett. **44**, 647 (1980).

[23] H. Laqua, V. Erckmann, H. Hartfuß, H. Laqua, and W7-AS ECRH Group, Phys. Rev. Lett. **78**, 3467 (1997).

[24] F. Volpe, H. Laqua, and W7-AS Team, Review of Scientific Instruments **74**, 1409 (2003).

[25] G. Taylor, P. Efthimion, B. Jones, T. Munsat, J. Spaleta, J. Hosea, R. Kaita, R. Majeski, and J. Menard, Review of Scientific Instruments **72**, 285 (2001).

[26] M. Easterling, T. Mize, and I. Amster, Analytical Chemistry **71**, 624 (1999).

[27] C. Masselon, A. Tolmachev, G. Anderson, R. Harkewicz, and R. Smith, Journal of the American Society for Mass Spectrometry **13**, 99 (2002).

[28] R. Wong and I. Amster, International Journal of Mass Spectrometry **265**, 99 (2007).

[29] E. B. Ledford, D. L. Rempel, and M. L. Gross, Analytical Chemistry **56**, 2744 (1984).

[30] R. W. Gould, Physics of Plasmas **2**, 1404 (1995).

[31] D. H. E. Dubin, Physics of Plasmas **20**, 042120 (2013).

[32] R. W. Gould and M. A. LaPointe, Phys. Rev. Lett. **67**, 3685 (1991).

[33] S. Barlow, J. Luine, and G. Dunn, International Journal of Mass Spectrometry and Ion Processes **74**, 97 (1986).

[34] D. Rempel, E. Ledford Jr, S. Huang, and M. Gross, Analytical Chemistry **59**, 2527 (1987).

[35] A. Peurrung, R. Kouzes, and S. Barlow, International Journal of Mass Spectrometry and Ion Processes **157**, 39 (1996).

[36] K. S. Fine and C. F. Driscoll, Physics of Plasmas **5**, 601 (1998).

[37] J. Jeffries, S. Barlow, and G. Dunn, International Journal of Mass Spectrometry and Ion Processes **54**, 169 (1983).

[38] R. Burton, K. Matuszak, C. Watson, and J. Eyler, Journal of the American Society for Mass Spectrometry **10**, 1291 (1999).

[39] D. H. E. Dubin, Phys. Rev. Lett. **79**, 2678 (1997).

[40] F. Anderegg, X.-P. Huang, C. F. Driscoll, E. M. Hollmann, T. M. O'Neil, and D. H. E. Dubin, Phys. Rev. Lett. **78**, 2128 (1997).

[41] D. H. E. Dubin and T. M. O'Neil, Phys. Rev. Lett. **78**, 3868 (1997).

[42] E. M. Hollmann, F. Anderegg, and C. F. Driscoll, Phys. Rev. Lett. **82**, 4839 (1999).

[43] C. F. Driscoll, J. H. Malmberg, and K. S. Fine, Phys. Rev. Lett. **60**, 1290 (1988).

[44] J. M. Kriesel and C. F. Driscoll, Phys. Rev. Lett. **87**, 135003 (2001).

[45] G. Andresen et al., Nature **468**, 673 (2010).

[46] G. Gabrielse, X. Fei, L. A. Orozco, R. L. Tjoelker, J. Haas, H. Kalinowsky, T. A. Trainor, and W. Kells, Phys. Rev. Lett. **63**, 1360 (1989).

[47] B. M. Jelenković, A. S. Newbury, J. J. Bollinger, W. M. Itano, and T. B. Mitchell, Phys. Rev. A **67**, 063406 (2003).

[48] A. M. Beloborodov and C. Thompson, The Astrophysical Journal **657**, 967 (2007).

[49] J. A. Boedo, D. L. Rudakov, R. A. Moyer, G. R. McKee, R. J. Colchin, M. J. Schaffer, P. Stangeby, W. West, S. L. Allen, T. E. Evans, et al., Physics of Plasmas **10**, 1670 (2003).

[50] Y. Liang, H. Koslowski, P. Thomas, E. Nardon, B. Alper, P. Andrew, Y. Andrew, G. Arnoux, Y. Baranov, M. Bécoulet, et al., Phys. Rev. Lett. **98**, 265004 (2007).

[51] B. LaBombard, J. Rice, A. Hubbard, J. Hughes, M. Greenwald, J. Irby, Y. Lin, B. Lipschultz, E. Marmar, C. Pitcher, et al., Nuclear Fusion **44**, 1047 (2004).

[52] A. Trivelpiece and R. Gould, Journal of Applied Physics **30**, 1784 (1959).

[53] J. R. Danielson, D. H. E. Dubin, R. G. Greaves, and C. M. Surko, Reviews of Modern Physics **87**, 247 (2015).

[54] F. Anderegg, M. Affolter, A. A. Kabantsev, D. H. E. Dubin, A. Ashourvan, and C. F. Driscoll, Physics of Plasmas **23**, 055706 (2016).

[55] A. Ashourvan and D. H. E. Dubin, Physics of Plasmas **21**, 052109 (2014).

[56] A. Lenard and I. B. Bernstein, Physical Review **112**, 1456 (1958).

[57] M. E. Glinsky, T. M. ONeil, M. N. Rosenbluth, K. Tsuruta, and S. Ichimaru, Physics of Fluids B **4**, 1156 (1992).

[58] M. Anderson and T. ONeil, Physics of Plasmas **14**, 112110 (2007).

[59] M. W. Anderson, T. M. ONeil, D. H. E. Dubin, and R. W. Gould, Physics of Plasmas **18**, 102113 (2011).

[60] G. Dimonte and J. Daligault, Phys. Rev. Lett. **101**, 135001 (2008).

[61] S. D. Baalrud and J. Daligault, Phys. Rev. Lett. **110**, 235001 (2013).

[62] A. Ng, L. Pitt, D. Salzmann, and A. A. Offenberger, Phys. Rev. Lett. **42**, 307 (1979).

[63] J. E. Bernard and J. Meyer, Phys. Rev. Lett. **55**, 79 (1985).

[64] S. H. Glenzer, L. M. Divol, R. L. Berger, C. Geddes, R. K. Kirkwood, J. D. Moody, E. A. Williams, and P. E. Young, Phys. Rev. Lett. **86**, 2565 (2001).

[65] C. E. Clayton, C. Joshi, and F. F. Chen, Phys. Rev. Lett. **51**, 1656 (1983).

[66] T. Chapman, R. Berger, S. Brunner, and E. Williams, Phys. Rev. Lett. **110**, 195004 (2013).

[67] R. Berger, S. Brunner, T. Chapman, L. Divol, C. Still, and E. Valeo, Physics of Plasmas **20**, 032107 (2013).

[68] T. Chapman, S. Brunner, J. Banks, R. Berger, B. Cohen, and E. Williams, Physics of Plasmas **21**, 042107 (2014).

[69] D. Pesme, C. Riconda, and V. Tikhonchuk, Physics of Plasmas **12**, 092101 (2005).

[70] B. Cohen, E. Williams, R. Berger, D. Pesme, and C. Riconda, Physics of Plasmas **16**, 032701 (2009).

[71] H. Bandulet, C. Labaune, K. Lewis, and S. Depierreux, Phys. Rev. Lett. **93**, 035002 (2004).

[72] C. Niemann, S. H. Glenzer, J. Knight, L. Divol, E. A. Williams, G. Gregori, B. I. Cohen, C. Constantin, D. H. Froula, D. S. Montgomery, and R. P. Johnson, Phys. Rev. Lett. **93**, 045004 (2004).

[73] H. Higaki, Plasma Physics and Controlled Fusion **39**, 1793 (1997).